A comparative study of CO_2–Ar potential surfaces

Marc A. ter Horst
Department of Chemistry, Northwestern University, Sheridan Road, Evanston, Illinois 60208-3113

Cynthia J. Jameson
Department of Chemistry M/C 111, University of Illinois at Chicago, Chicago, Illinois 60607-7061

(Received 9 May 1996; accepted 11 July 1996)

Twelve potential energy surfaces that have been proposed for the CO_2–Ar interaction have been considered in detail. The anisotropies of these surfaces are compared and their ability to predict the interaction second virial coefficient as a function of temperature has been examined. Intermolecular bending and stretching quadratic force constants predicted by each and the mean square torque calculated for each are compared with the experimental values. Quantum diffusion Monte Carlo simulations provide the average rotational constants and geometry for the ground vibrational state as well as the dissociation energy in each case. These are compared with the experimental values. Classical trajectory calculations were carried out to obtain 45 types of thermal average cross sections for six of these surfaces. Various thermophysical properties such as mixture viscosity, mixture thermal conductivity, and diffusion coefficient, calculated from these cross sections and the NMR relaxation cross sections, are compared with experimental data. It is found that the spectroscopic constants define the depth and shape of the well at the global minimum, whereas the NMR cross sections and mean square torque probe the anisotropy in a broader sense. The thermophysical properties (viscosity, diffusion coefficient, and thermal conductivity) are not strongly discriminating between the surfaces, whereas the temperature dependence of the second virial coefficient detects the weaknesses in the low and upper repulsive walls of those surfaces that were modified specifically to improve greatly the shape of the well so as to reproduce the spectroscopic constants. © *1996 American Institute of Physics.* [S0021-9606(96)01439-0]

I. INTRODUCTION

There is considerable current interest in the CO_2–Ar system, a good model system for understanding the interactions between an atom and a linear triatomic molecule and energy transfer dynamics. Originally, scattering data and potential energy surface calculations predicted a T-shaped equilibrium geometry.[1,2] The Ar–CO_2 van der Waals complex was first identified by Steed, Dixon, and Klemperer, who confirmed the T-shaped configuration by molecular beam electric resonance spectroscopy.[3] The dipole moment of this complex has also been determined precisely from a measurement of the Stark effects on the rotational transitions. From the centrifugal distortion constants the force constants for the stretch and bend of the weak bond were obtained. The vibrational frequencies corresponding to these were calculated by normal coordinate analysis.[3] The ground state rotational constants obtained by optothermal infrared spectroscopy were in good agreement with those reported by Steed, Dixon, and Klemperer and the stretch and bend harmonic frequencies derived were 37.5 and 29.4 cm^{-1}.[4] The observation of the vibration–rotation spectra for rare-gas CO_2 clusters in the vicinity of the CO_2 asymmetric stretching band in the infrared permitted a more accurate determination of the A rotational constant as the ir transitions provide direct information on A via transitions that are microwave forbidden.[5] The van der Waals bending frequency (27.8 cm^{-1}) has been determined experimentally by observation of the combination band of the asymmetric stretch of the CO_2 and the intermolecular bend.[6] The photofragment angular distributions resulting from vibrational predissociation of the CO_2–Ar complex from both members of the $(101)/(02^01)$ Fermi diad have been reported.[7] Since all of the angular distributions must be accounted for by the same value of the dissociation energy, the assignment of the final state distributions in this work has permitted the determination of the an accurate value for the dissociation energy of the complex. $D_0=166$ cm^{-1} yielded an energy level pattern which was consistent with the experimental results.[7] Earlier estimates of D_0 based on microwave spectroscopy[4] and molecular beam scattering.[1,8] ranged from 136 to 220 cm^{-1}.

Broadening coefficients for individual vibration–rotation lines of CO_2 in Ar have been measured experimentally by Joyner *et al.*[9] Measurements of spectral moments of the infrared vibration–rotation bands of CO_2 provided the mean square torque as a function of Ar density,[10] and the collision-induced absorption of CO_2 in Ar originating from the dipole moments induced in the pair have been observed,[11–13] providing the temperature-dependent spectral moments of the low density absorption coefficient which are spectral invariants, depending on the pair dipole moment and intermolecular potential. The interaction second virial coefficients have been measured over a range of temperatures,[14,15] and the usual thermophysical properties (mixture viscosity[16,17] and thermal conductivity[18]) have been reported as a function of composition and temperature, and diffusion coefficients as a function of temperature.[19–22] Several potential energy surfaces (PES's) have been proposed and fitted to one or more of these observables,[1,7,23–30] but a comprehensive compari-

son of these potential surfaces with respect to their predictions of thermophysical properties and spectroscopic data has not yet been presented.

In this article, we compare the ability of these potential surfaces to predict experimental interaction second virial coefficients, diffusion coefficients, mixture viscosity, thermal conductivity, NMR relaxation cross sections, mean square torque, average rotational constants, intermolecular bending and stretching force constants, harmonic frequencies for the intermolecular bending and stretching, and dissociation energy for the Ar–CO_2 complex. We use a combination of classical trajectory calculations and quantum diffusion Monte Carlo techniques to investigate these various experimental observables, all of which are sensitive to the intermolecular potential surface in different ways. We also use close coupling calculations on one PES at a very low total energy to provide a check on the classical trajectory results.

II. METHODS

A. Classical calculations of the collision cross sections

McCourt and co-workers have provided a detailed derivation of the collision cross sections related to the transport and relaxation properties which are used in testing nonreactive potential surfaces.[31,32] From the Boltzmann equation, the Chapman–Enskog procedure[33] can be used to obtain classical definitions of the kinetic theory cross sections (see also Refs. 34 and 35). The nomenclature used to label the collision cross sections specifies the nature of the collisional process which contributes to the phenomenon. In general, a collision or effective cross section is given by

$$\mathfrak{S}\left(\begin{array}{cccc|c} p & q & s & t & k \\ p' & q' & s' & t' & k' \end{array}\right)_{kk'}.$$

The indices p,q,s,t represent the precollisional (primed) and postcollisional (unprimed) tensorial ranks or powers of the microscopic polarizations which are coupled. p denotes the p-fold tensor and product of the reduced peculiar velocity $\mathbf{W}=(m/2k_BT)^{1/2}(\mathbf{v}-\mathbf{v}_0)$, for a gas flowing with velocity $\mathbf{v}_0$, and q denotes the tensorial rank in the molecular angular momentum $\mathbf{j}$. The s and t indices denote the scalar dependences of the cross section on the translational and reduced rotational energy. The various k's label to which collision partner the polarizations belong. When the pre- and postcollisional values are identical and changes in only one partner are relevant, the cross section can be abbreviated, $\mathfrak{S}(pqst|k)_{kk''}$. Henceforth, in this article we will use the symbol σ instead of $\mathfrak{S}$ to designate these cross sections.

The thermal average cross sections were calculated for the various PES's from fully classical trajectories (CT) using the code developed by Dickinson and Lee[36] without any modifications. Wong has described this code in detail.[37] In a study of the N_2–He system,[38] it gave results similar to those of the close-coupling method, the agreement improving with increasing temperature, as more rotational states of N_2 are occupied. The classical approach and the Dickinson–Lee code are-expected to provide accurate results for the CO_2–Ar as it did with N_2–Ar and N_2–Kr systems.[39–41]

The rigid rotor approximation and action angle coordinates can be used to reduce the set of variables used as initial conditions, as in

$$H(P,l,j;R,q_l,q_j)=(P^2+l^2/R^2)/2\mu+Bj^2+V(R,\cos\,\theta), \tag{1}$$

where P is the center-of-mass momentum, R is the separation of centers of mass of the colliding species, and μ is the reduced mass. The orbital angular momentum l is defined as the angular momentum of the atom about the center of mass of the rotor. The rotational energy of the rotor is given by the rotational constant B and angular momentum $\mathbf{j}$. The potential energy function $V(R,\cos\theta)$ is written in terms of R and the cosine of the angle θ between the rotor axis and the line of centers. Details of the system coordinates and their respective integration can be found elsewhere.[37,29,42,43]

Convergence was checked by comparing energy-dependent cross sections which are related by time-reversal symmetry (TRS). TRS cross sections are related by their similar dependence on the initial and final velocities and angular momenta. For example, the following energy-dependent production cross sections are related by whether the dependence is on the initial velocity $\mathbf{v}'$ and final angular momentum $\mathbf{j}$ or on $\mathbf{v}$ and $\mathbf{j}'$,

$$\sigma(02|20)_{[E_{\rm tot}]}=\int\langle P_2(\mathbf{v}'\cdot\mathbf{j})\rangle_E d\tau \tag{2}$$

and

$$\sigma(20|02)_{[E_{\rm tot}]}=\int\langle P_2(\mathbf{v}\cdot\mathbf{j}')\rangle_E d\tau, \tag{3}$$

where $d\tau$ is the integration element for the averages over ω and b, where ω represents the partitioning of the total energy $E_{\rm tot}$ into rotational energy E_r and translational (or kinetic) energy E_k, $\omega=(E_r-E_k)/E_{\rm tot}$, and b is the impact parameter. The integrand or opacity function represents the functional description of the collision process averaged over initial relative orientations. A similar nomenclature to that for thermal average cross sections is used to denote the pertinent polarizations in these energy-dependent functions. The inverted order of the indices identifies TRS cross sections. Additional comparisons can be made between two cross sections that depend on the same collisional process but involve different functional forms. These cross sections differ in the explicit form of the opacities used. The viscosity cross section $\sigma_\eta^{(2)}$ is calculated with two functionally different opacity functions and these are also used to test for convergence. From Wong's work on several linear-molecule–atom systems, the viscosity cross sections were found to disagree only at low temperatures and by less then 0.1%.[31] The disagreement found in the initial pass on the CO_2–Ar surfaces was approaching 1% at 300 K, when six to eight points were used

in each of the three orientation angles. We found that agreement improved upon increasing these to 12 points and by more careful selection of b_r.

On the order of 5 million trajectories were run on the CO_2–Ar surfaces. All calculations were carried out on IBM RISC/6000 model 560 and model 365 workstations.

B. Close-coupling calculations

It was thought that the disagreement between the cross sections that are related by time-reversal symmetry in the CO_2–Ar calculations might be caused by the occurrence of orbital resonances or by van der Waals (vdW) dimers formed within the trajectory. These structures will result in failed trajectories and a zero contribution from the set of initial conditions. If vdW complexes caused enough trajectories to be stuck in a loop and terminate, the resultant cross sections will be averaged incorrectly and may result in violations of time-reversal symmetry. To check this possibility, close-coupling (CC) calculations were made on one CO_2–Ar surface at a total energy of 40 cm^{-1}. The CC method involves the solution of the Schrödinger equation in which the PES influences the coupling of the many possible states of the system.[44] For the linear, rigid-rotor–atom system the wave functions are defined for discrete values of the total energy E and the rotational quantum numbers j and m_j and as a continuous function of the center-of-mass separation R and the orientations of the vector joining the centers of mass and the symmetry axis of the rotor. The wave functions are used to calculate the scattering amplitude, which is related to a summation over the elements of the scattering matrix. The scattering matrix elements $S^J(j'l',jl)$ for J, j, and l, the total angular momentum, the rotor angular momentum, and the orbital angular momentum, provide the information needed to calculate the probability that a transition between any two states $j'l'$ and jl will occur. The CC method requires the calculation of the radial dependence of the wave function for all possible rotational states, so that all possible open channels are explored. Since the number of coupled equations varies as $(j_{\max})^2$ and the computational effort as the number of equations cubed, the overall demands on computer time varies as $(j_{\max})^6$.[45] Thus, the CC method is not convenient for a full calculation of the thermal average cross sections of the CO_2–Ar system, although it is possible to study it at low total energies. It is just the trajectories at low total energy that are suspected of being adversely affected by orbital resonances or formation of vdW dimers. Therefore, we carried out CC calculations for one potential surface at $E=40$ cm^{-1} for $j=0,2,4,6,8$. Only half of the channels need to be considered, since the total wave function has to be symmetric with respect to interchange of two nuclei of spin 0, and therefore only the $j=$even rotational states are populated for O $^{16}O_2$ molecules. Calculations were conducted at the University of Waterloo, Ontario, Canada using Hutson and Green's MOLSCAT (version 11) program[46] with the assistance of Fred McCourt and Carey Bissonnette. The j weighting factors were the ones used by Liu, McCourt, and Dickinson for their comparison of CC and CT calculations of HD–He collision cross sections.[47] Six energy-dependent cross sections have been calculated for CO_2–Ar: $\sigma_\eta^{(1)}$, $\sigma_\eta^{(2)}$, σ_{DPR} (which is equivalent to the NMR cross section $\sigma_{\theta,2}$ in this case), σ_T, $\sigma_{T\eta}$, and $\sigma_{\eta T}$.

C. Quantum diffusion Monte Carlo method

Among the techniques that may be applied to the vibrational dynamics of a weakly bound complex is quantum diffusion Monte Carlo (QDMC). Anderson gave the first modern algorithm for simulating the Schrödinger equation as if it were a diffusion process.[48] The simulation consists of a number of copies of the system. Each copy is allowed to diffuse via a random walk process and to multiply or disappear with a probability determined by its potential energy. This process is repeated until the distribution of replicas approaches a fluctuating steady state from which the ground state energy is evaluated. After equilibration, the simulation yields a collection of replicas of the system that have the statistical distribution which approaches the ground state wavefunction of the system. Buch has implemented QDMC for two or more interacting molecules, each taken to be rigid, which we adopt here with no changes.[49] This treatment relies on the approximation that the high frequency intramolecular vibrations are effectively decoupled from the lower frequency intermolecular motions because these two types of motions occur at very different time scales. By eliminating the high frequency motions the number of variables is decreased and larger time steps may be taken. Our simulations consisted of an equilibration phase lasting 600 time steps before the data collection phase. The number of replicas in all calculations was 5000. In each QDMC run the first 600 steps were carried out with a time step of 130–200 a.u. after which the time step was decreased to 30 a.u. It is important that the first steps on the simulation are done with long enough time steps to probe a large region of the PES. Rotational constants and all other properties averaged over the zero-point motion were calculated by the method of descendant weighting which provides the means of obtaining expectation values from the distribution generated by QDMC.[50,51] The descendant weighting procedure used to obtain the averages was adopted from Ref. 52. The averaging was performed for 12 generations of replicas simultaneously at a delay of 100 steps between the consecutive generations. The descendants were collected after a delay of 500 steps for 1000 steps. The ground state energy is obtained from the requirement of stability of the asymptotic average number of replicas. For a given potential energy surface of CO_2–Ar, from the QDMC simulations we obtain the average rotational constants A, B, C for the ground vibrational state and the ground state zero-point energy (and thus the dissociation energy D_0). These average quantities will be compared with the experimental values.[3,7]

III. POTENTIAL FUNCTIONS FOR CO_2–Ar

We have used several different models of intermolecular potentials which have been proposed for the CO_2–Ar system in the literature. We briefly describe them here. These potential functions differ considerably in the amount of anisot-

ropy. We also used a new potential energy surface based on a fit to fundamental components of the PES that have been recently calculated using supermolecular Moller–Plesset perturbation theory.[30]

An isotropic PES for CO_2–Ar based on the corresponding states has been provided by Maitland *et al.*[53] This is based on the hypothesis that the intermolecular potentials for a number of pair interactions can be rendered conformal by the choice of two scaling factors ϵ_c and σ_c characteristic of each interaction. In the correlations of thermophysical properties such as viscosity, diffusion coefficient, and thermal conductivity, the scaling parameters of the supposed conformal potential have been chosen so that ϵ_c and σ_c for argon are consistent with well depth and the separation at zero potential energy of the Aziz potential for argon.[54] Although this isotropic potential reproduces reasonably well the experimental moments γ_1 and α_1 of the collision-induced absorption coefficients of CO_2–Ar mixtures at various temperatures,[55] and the scaling parameters had been based on experimental mixture viscosity, diffusion coefficient, and thermal conductivity, we do not consider it further because it cannot explain quantities that explicitly depend on the anisotropy of the potential surface.

Loesch fitted a site-to-site LJ(12,6) form (LJ denotes Lennard-Jones) to detailed integral cross sections from molecular beam scattering results.[1] The potential was written as a sum of two LJ(12,6) functions to describe the oxygen–argon interaction

$$V(R)/\epsilon=(R_m/r_a)^{12}-2(R_m/r_a)^6+(R_m/r_b)^{12}-2(R_m/r_b)^6, \tag{4}$$

where r_a and r_b are the distances from the argon atom to each of the oxygen nuclei in CO_2. Calculations using the infinite order sudden approximation (IOSA) on the Loesch surface by Rotzoll and Lübbert (RL) failed to show the experimentally observed rainbow, attributed to the relatively strong anisotropy in the attractive part of the Loesch function.[24]

Two electron gas model potentials (PPI and PPII) were proposed by Pack and co-workers.[2,23] Within this model, the potential energy is calculated from the charge density ρ_{AB} of the supermolecule which is approximated as the sum of the charge densities of each molecule, $\rho_{AB}=\rho_A+\rho_B$. Calculated values of the dispersion coefficients C_6 and C_8 were used.[56] In one version of the surface (PP1) the Hartree–Fock (HF) terms were scaled down to agree with experimental second virial coefficients $B_{12}(T)$ while in the other, the correlation terms were scaled up (PP2). The isotropic repulsive wall of the PP1 surface was shown to agree with previous scattering data in the range of $V_0(R)=0.04$ to 0.1 hartree.[57] Comparison with Loesch's molecular beam experiments[1] using a semiclassical trajectory approach on both PP1 and PP2 surfaces led to good agreement for the integral cross section, but PP1 did a better job of reproducing the angular distributions. The pressure-broadened dipole and Raman lines were calculated within the IOSA approximation using these surfaces.[58] Agreement is much better at small j, and the discrepancy for large j is in accord with the limitations of the IOSA. IOSA calculations of the total laboratory differential cross section on the PP1 surface failed to show the experimentally observed rainbow.[24] It was stated that the discrepancy is due to the relatively strong anisotropy in the attractive part of these surfaces. The PP2 surface produces a rainbow but at larger angles than in the experiment.

Another potential function that has been used to describe a linear rotor–atom system is an anisotropic LJ(12,6) potential of the form proposed by Pack,[59]

$$V(R,\theta)=\epsilon(\theta)\{[R_m(\theta)/R]^{12}-2[R_m(\theta)/R]^6\}, \tag{5}$$

where

$$\epsilon(\theta)=\overline{\epsilon}[1+aP_2(\cos\ \theta)], \quad R_m(\theta)=\overline{R_m}[1+bP_2(\cos\ \theta)].$$

The cosine-averaged quantities, $\overline{\epsilon}$ and $\overline{R_m}$, provide the isotropic contribution to the interaction energy, while the parameters a and b control the anisotropy. Rotzoll and Lübbert (RL) used this functional form for the CO_2–Ar system, adjusting the parameters to reproduce their experimental values for the total laboratory differential cross section.[24] Values reported for R_m and b are only estimates since there were no observations of the rapid, diffraction oscillations. Values for $\overline{\epsilon}$ and a were reported to 5% and at least 50% uncertainty, respectively.

Berreby and Dayan (BD) used experimental values of the mean square torque to derive an anisotropic LJ(12,6) type surface for a number of linear rotor–atom systems.[25] Using the first two nonzero terms in the Legendre expansion, $V(R,\theta)=V_0(R)+V_2(R)P_2(\cos\theta)$, the isotropic radial part is written in the usual LJ(12,6) form with the well depth and σ parameters determined from combining rules. For the anisotropic part, a modified form was used,

$$V_2(R)=4\epsilon[\delta(\sigma/R)^{12}-\gamma(\sigma/R)^6]. \tag{6}$$

The dispersion term has been suggested by Buckingham,[60] where γ is the anisotropy of polarizability of the active molecule, i.e., CO_2. The repulsive term has been suggested by Gordon,[61] where the parameter δ was adjusted so that the experimental values for $\langle C^2\rangle$ were reproduced. It was found that δ depended on the active molecule alone and very similar values for δ were found for NNO, CO_2 and OCS.[25]

Billing combined electron gas calculations of Dreyfus[62] and the dispersion coefficients calculated by Pack[56] to build a CO_2–Ar surface as follows:[26]

$$V(R,\theta)=V_{\rm sr}^0(1-h)+hV_{\rm LR}. \tag{7}$$

The short range energy, $V_{\rm sr}^0$, was fitted to the results of the electron gas calculation using

$$\begin{aligned} V_{\rm sr}^0(R,\theta)&=A[\exp(-\alpha R_1)+\exp(-\alpha R_2)]\\ &\quad +B\ \exp(-\beta R),\\ R_1&=R+d\ \cos\ \theta+(d^2/2R)\sin^2\ \theta,\\ R_2&=R-d\ \cos\ \theta+(d^2/2R)\sin^2\ \theta,\\ \alpha&=\alpha_0+\alpha_1 R+\alpha_2 R^2. \end{aligned} \tag{8}$$

The distances R_1 and R_2 are the separations of the argon atom and each of the oxygen atoms, d is the C–O bond distance, R is the Ar–C distance, and the parameters $(\alpha_0,\alpha_1,\alpha_2,A,B,\beta)$ were varied in the fit. The long range part

$$V_{\mathrm{LR}}(R,\theta)=-\sum_{n=5,8}^{n-4} R^{-n}\sum_{k=0,2} C_n^{(k)}P_n(\cos\ \theta) \tag{9}$$

was obtained from the calculations by Pack.[56] The parameters a and d in the switching function, $h=\exp[-a(d/R-1)^2]$, were adjusted so that experimental B_{12} values were reproduced. This surface was used to analyze the high energy/small angle differential cross sections from molecular beam data.

The BTF potential proposed by Bulanin, Tonkov, and Filipov is an anisotropic potential derived from measurements of the pressure-broadened high frequency wing of the asymmetric stretch of CO_2.[27] The potential function is in the following form:

$$V/k_BT=-200/T+[6.1\ \cosh(6.1\ \cos\ \theta)\sinh(6.1)]$$
$$\times\exp[\ln(1.4\times10^8/T)-R/0.30],$$

with T in kelvins and R in Å. The parameters in this potential were obtained by comparison with the PP2 surface.

Using a simultaneous least squares method,[63] Hough and Howard fitted four different versions of the Maitland–Smith $(n-6)$ potential function[28]

$$V(R)=[\epsilon/(n-6)](6x^{-n}-nx^{-6}),$$
$$n=m+9(x-1),\quad x=R/R_m \tag{10}$$

to data from molecular beam electric resonance spectra, interaction second virial coefficient B_{12}, and mean square torque $\langle C^2\rangle$ measurements. The angular dependence was included in two different ways. In the three angle parametrization (referred to as 3A), the surface was expanded in even-order Legendre polynomials up to $P_4(\cos\theta)$. The radial parts are written as sums of the cuts through the surface at θ=0°, 60°, and 90°:

$$V_0(R)=[7V(R,0°)+32V(R,60°)+6V(R,90°)]/45,$$
$$V_2(R)=2[17V(R,0°)+16V(R,60°)-32V(R,90°)]/63, \tag{11}$$
$$V_4(R)=32[V(R,0°)-4V(R,60°)+3V(R,90°)]/105.$$

The angle-dependent parametrization (referred to as AD) writes the well depth parameters in a Legendre expansion,

$$R_m(\theta)=\sum_{n=0,2,4}(R_m)_nP_n(\cos\ \theta),$$
$$\epsilon(\theta)=\sum_{n=0,2,4}(\epsilon_m)_nP_n(\cos\ \theta), \tag{12}$$

and uses the $(n-6)$ form for the radial dependence, with $\epsilon=\epsilon(\theta)$ and $R_m=R_m(\theta)$. Within each of these parametrizations, two other surfaces (3A-M and AD-M) were constructed by allowing m in the Maitland–Smith form to vary. The properties they used in the fits are most sensitive to the attractive region of the PES with the exception of the mean square torque, which has been shown to depend on the angular derivative of the entire surface.[64] Of the four surfaces they considered, we choose the 3A and AD-M to include in our comparisons.

Using more recent spectroscopic data, Miller and coworkers refitted the 3A-M and AD-M surfaces.[7] The two new surfaces, 3A-R and AD-R, have similar well depth parameters but their repulsive walls are much weaker in comparison with the original surfaces. It has been suggested by Miller and co-workers[65] that a double global minimum as a function of θ (at one value of R) may be expected for larger linear rotor–atom systems. The double minimum structure had been found to be necessary to reproduce the intermolecular bending frequency determined from ir spectra of the HCCH–Ar complex.[65] The *ab initio* calculations on the CO_2–Ar system did not reveal any such double minima, however.[30]

Iida, Ohshima, and Endo[29] used a functional form with only $P_2(\cos\theta)$ angular dependence, with parameters based entirely on spectroscopic data

$$V(r,\theta)=[C_{12}^{(0)}+C_{12}^{(2)}P_2(\cos\ \theta)]r^{-12}$$
$$-[C_6^{(0)}+C_6^{(2)}P_2(\cos\ \theta)]r^{-6}$$
$$-(9/2)Q^2\alpha_{\mathrm{Ar}}[P_2(\cos\ \theta)]^2r^{-8}, \tag{13}$$

where $r=R/R_m$, $C_6^{(2)}=C_6^{(0)}(\alpha_\parallel-\alpha_\perp)/(\alpha_\parallel+2\alpha_\perp)$, and $C_6^{(0)}$ is determined experimentally from the frequency-dependent polarizabilities.[66] The coefficients $C_{12}^{(0)}$ and $C_{12}^{(2)}$ were adjusted to the stretching and bending force constants of the T-shaped van der Waals complex.

Finally we test also the new *ab initio* PES for CO_2–Ar which has been fitted to analytic functions of the form[30]

$$V(R,\theta)=V_{\mathrm{sr}}+V_{\mathrm{ind}}+V_{\mathrm{disp}}, \tag{14}$$

where

$$V_{\mathrm{sr}}=A'\ \exp\{-\beta(\theta)[R-R_{\mathrm{ref}}(\theta)]\},$$
$$R_{\mathrm{ref}}(\theta)=\sum_L\ R_{\mathrm{ref},L}P_L(\cos\ \theta), \tag{15}$$
$$\beta(\theta)=\sum_L\ \beta_LP_L(\cos\ \theta),$$
$$V_{\mathrm{ind}}=-\sum_{n=8}^{10}\sum_{L=0}^{n-4}R^{-n}C_{n,\mathrm{ind}}^{(L)}P_L(\cos\ \theta),$$
$$V_{\mathrm{disp}}=-\sum_{n=6}^{10}\sum_{L=0}^{n-4}D_n(\beta,R)R^{-n}C_n^{(L)}P_L(\cos\ \theta), \tag{16}$$
$$D_n(\beta,R)=1-\exp[-\beta(\theta)R]\sum_{k=0}^{n}[\beta(\theta)R]^k/k!. \tag{17}$$

The points of interest on each of the surfaces are the energy minima at the perpendicular (θ=90°) and parallel (θ=0°) configurations of the CO_2–Ar dimer and the values of σ

TABLE I. Characteristics of the CO_2–Ar surfaces.[a]

PES	RL	PP1	PP2	3A	AD-M	3A-R	AD-R	Billing	Loesch	BD	*Ab initio*
Reference	24	23	23	28	28	7	7	26	1	25	30
ϵ (90°)	132.2	278.7	144.3	201.8	186.8	196.4	196.3	175.95	155.34	175.74	210.0
R_m(90°)	3.420	3.272	3.548	3.442	3.446	3.455	3.444	3.518	3.618	3.942	3.475
σ (90°)	3.05	2.89	3.14	3.07	3.09	2.911	2.890	3.130	3.180	3.512	3.069
ϵ (0°)	113.3	44.6	129.5	57.0	57.0	57.0	57.0	131.51	86.37	81.576	113.0
R_m(0°)	4.56	4.93	4.57	4.90	5.00	5.00	5.00	4.239	4.941	4.771	4.708
σ (0°)	4.06	4.50	4.19	4.37	4.48	4.213	4.196	3.915	4.525	4.251	4.281
$\Delta\epsilon$	18.90	234.1	14.8	144.8	129.8	139.4	139.3	44.44	69.0	94.16	97.0
ΔR_m	1.14	1.66	1.02	1.46	1.55	1.545	1.556	0.72	1.323	0.829	1.233
$\Delta\sigma$	1.01	1.61	1.05	1.30	1.39	1.30	1.31	0.785	1.345	0.739	1.212
ΔR_{1000}	0.876	1.241	1.035	0.853	0.976	0.507	0.477	0.805	1.27	0.508	1.089
ΔR_{5000}	0.785	1.174	1.056	0.651	0.787	0.125	0.054	0.858	1.285	0.424	1.053

[a]Energies are in cm^{-1} and distances are in Å.

(where $R=\sigma$ corresponds to $V=0$) for these configurations. The anisotropies are expressed as the difference between a characteristic of the $\theta=0°$ and $\theta=90°$ cuts

$$\Delta\sigma=\sigma(\theta=0°)-\sigma(\theta=90°), \tag{18}$$

$$\Delta R_m=R_m(\theta=0°)-R_m(\theta=90°), \tag{19}$$

$$\Delta\epsilon=\epsilon(\theta=0°)-\epsilon(\theta=90°), \tag{20}$$

$$\Delta R_V=R_V(\theta=0°)-R_V(\theta=90°), \tag{21}$$

where $R_V(\theta)$ is the distance corresponding to a potential energy of V at a particular angle θ. A summary of the potential characteristics for these CO_2–Ar potentials are listed in Table I. Following Ref. 39, we characterize the anisotropy of the PES not only with the values of R_m, ϵ, and the crossing point σ at the two extremes ($\theta=0°$ and $\theta=90°$), which represent the linear and perpendicular geometries of the complex, but also include the values of the differences in position of the repulsive wall of the PES at the two extreme geometries for two energies $V=1000$ and 5000 cm^{-1} to provide an indication of the anisotropy for $R<\sigma$.

Cuts of the surfaces considered here are shown in Figs. 1 and 2. In the process of developing a global potential energy surface by fitting a functional form to a set of experimental data, attention must also be directed to the parts of the surface to which the data are not particularly sensitive. Bohac, Marshall, and Miller state that their modifications to the 3A and AD-M surfaces (3A-R and AD-R) are intended to describe the bowl of the surface,[7] so it is not surprising that the repulsive wall is much softer than the other CO_2–Ar surfaces.

For the CT study we chose six surfaces, RL, PP1, PP2, 3A, AD-M, and the new analytic function fitted to the *ab initio* surface. The PP1 and PP2 surfaces represent two extremes in which surfaces can be created within electron gas theory. The angle-averaged well depths of these surfaces are very similar, so that the pair provides a convenient means of comparing how two drastically different well anisotropies affect energy transfer. Of the four surfaces proposed by Hough and Howard, the 3A and AD-M surfaces have been promoted as the more reliable ones. Indeed, the basic way in which the anisotropy is written for these surfaces may manifest itself differently in the cross sections for thermophysical properties and relaxation. Since the mean square torque $\langle C^2\rangle$ is thought to be related to the repulsive wall anisotropy,[67] the use of mean square torque data in the fitting of the 3A and AD-M surfaces suggests that these surfaces are particularly promising for predicting the NMR cross sections.[68]

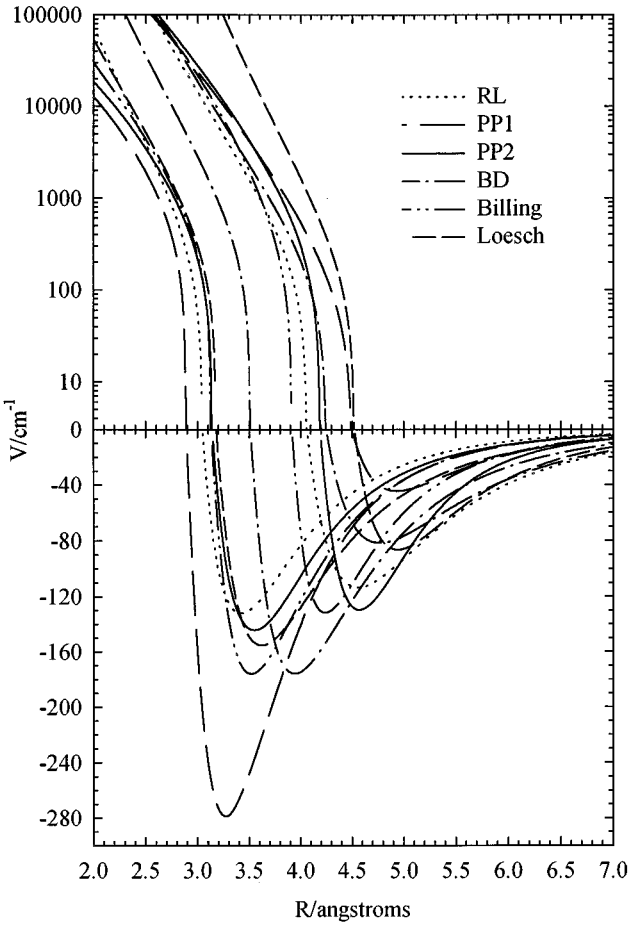

FIG. 1. Cuts at 90° and 0° of the RL, PP1, PP2, BD, Billing, and Loesch surfaces for CO_2–Ar.

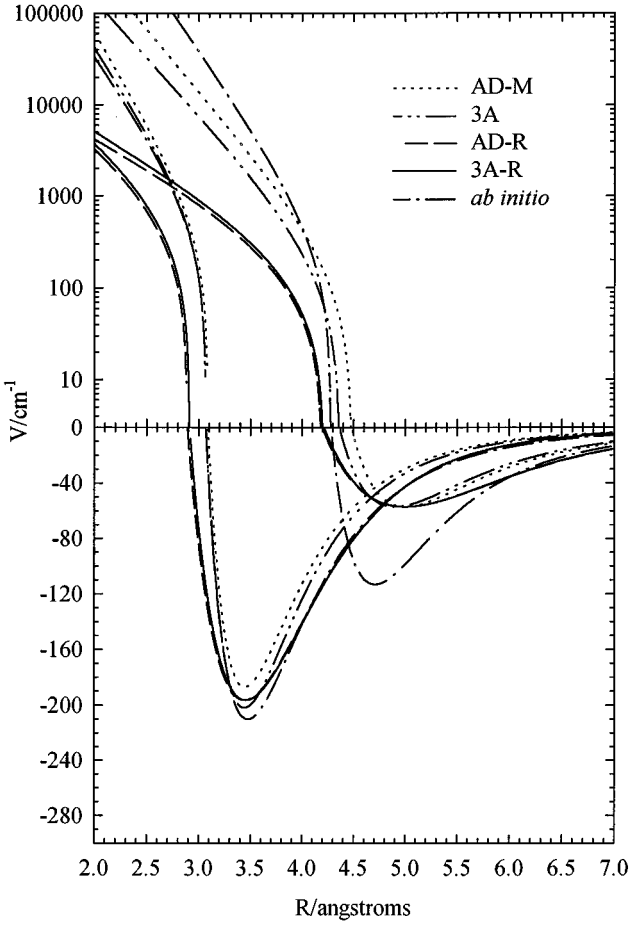

FIG. 2. Cuts at 90° and 0° of the AD-M, 3A, AD-R, 3A-R, and *ab initio* surfaces for CO_2–Ar.

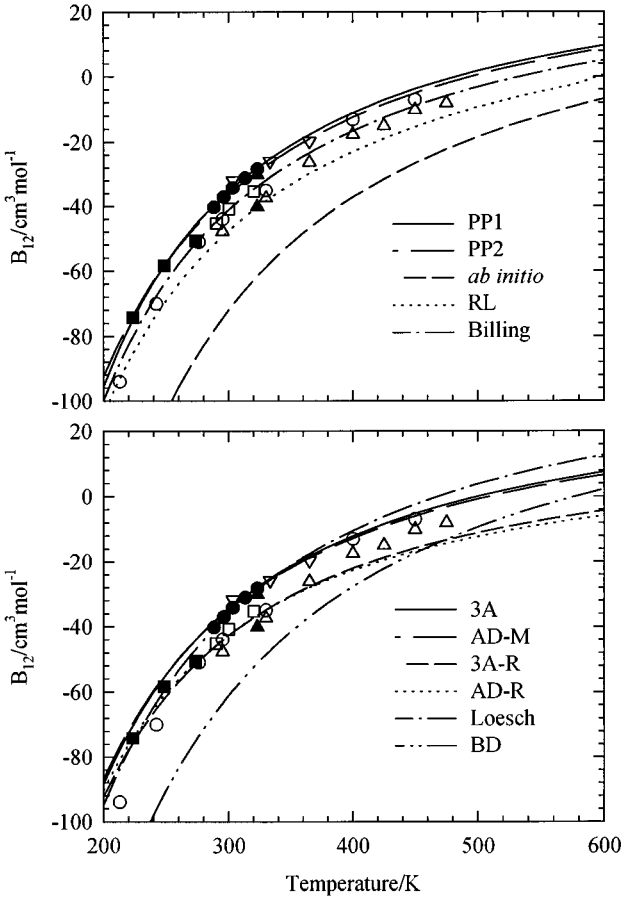

FIG. 3. Temperature dependence of the interaction second virial coefficient for CO_2–Ar calculated using various surfaces compared with experimental data: ●, Lichtenthaler and Schafer (Ref. 72); ■, Brewer (Ref. 15); ▲, Sutter and Cole (Ref. 73); ○, Schramm (Ref. 74); □, Martin *et al.* (Ref. 71); △, Ref. 11 in Hough and Howard (Ref. 63); ▽, Cottrell, Hamilton, and Taubinger (Ref. 14).

IV. RESULTS

A. Second interaction virial coefficients for CO_2–Ar

As in our previous study of N_2–Kr,[40] the interaction second virial coefficient B_{12} has been calculated as a function of temperature as follows:

$$B_{12}(T)=B_{12}^{\text{class}}(T)=N_0\pi\int_0^\infty R^2dR\int_{-1}^{1}d\cos\theta \times\{1-\exp[-V(R,\theta)/k_BT]\}. \quad (22)$$

The first translational and rotational quantum corrections were also included.[69,70] Figure 3 shows that most of the surfaces give reasonably good agreement with experiment over the entire range of temperatures. The PP1 and PP2 potentials reproduce the experimental values of Cottrell, Hamilton, and Taubinger[14] and Brewer[15] since they were adjusted to do so. Likewise, the Hough and Howard surfaces 3A and AD-M agree well due to the inclusion of B_{12} values[71–74] in their fitting procedure. Since B_{12} values were used in the determination of the Billing surface, the agreement is expected. Unfortunately, we could not reproduce exactly the B_{12} values published with the Billing surface.[26] (It should be noted that the value of the parameter d is 5.216 Å, not 5.16 Å as originally published.[75]) The revised Hough and Howard potentials (3A-R and AD-R) agree with experimental data at low temperature but deviate systematically, being progressively worse at the higher temperatures. The poor prediction of the temperature dependence of B_{12} is indicative of the weak repulsive wall of these revised surfaces. The *ab initio* and the Berreby–Dayan (BD) surfaces do the worst job by underestimating B_{12}, and BD also gives the wrong temperature dependence.

B. Spectroscopic constants and QDMC results

Collision-induced spectra originate from the dipole moments induced in clusters of molecules as a result of intermolecular interactions. Collision-induced microwave absorption in a nonpolar gas was first reported in compressed CO_2.[76] Later, Dagg *et al.*, working at 2.3 cm^{-1}, measured the absorption of CO_2 mixed with Ar.[12] In the low density limit the absorption depends on the product of the densities. The spectral invariants are the spectral moments γ_1 and α_1 for the absorption intensity, defined in terms of the absorption coefficient $\alpha(\omega)$ as[77]

$$\alpha_1=(\rho_{CO_2}\rho_{Ar})^{-1}\int_0^\infty \alpha(\omega)d\omega, \tag{23}$$

$$\gamma_1=(\rho_{CO_2}\rho_{Ar})^{-1}(\hbar/2k_BT)\int_0^\infty \alpha(\omega)d\omega \times[\omega\ \tanh(\hbar\omega/2k_BT)]^{-1}. \tag{24}$$

The experimental values of γ_1 and α_1 have been reported as a function of temperature.[11–13] Borysow and Moraldi analyzed the collision-induced absorption spectra (CIA) of CO_2–Ar mixtures.[55] They calculated the spectral moments from the PP1, PP2, RL, Billing, and BTF potentials, assuming the pure multipolar induction for the pair dipole moment.[55] It was found that only the PP2 surface (and the BTF potential derived from it) gave reasonable agreement with experimental values of α_1 and γ_1.

Mean square torque values were reported for the CO_2–Ar system by Dreyfus, Berreby, and Dayan.[10] The mean square torque $\langle C^2\rangle$ is related to the second and fourth spectral moments of the absorption profile $I(\nu)$ of an ir absorption band,[10]

$$\langle C^2\rangle=[M(4)-2M^2(2)]/4B^2, \tag{25}$$

where

$$M(n)=\int(\nu-\nu_0)^nI(\nu)d\nu. \tag{26}$$

These are related to the dipole correlation function $\langle\mathbf{u}(0)\cdot\mathbf{u}(t)\rangle$ by

$$\langle\mathbf{u}(0)\cdot\mathbf{u}(t)\rangle=\int I(\nu)\exp[2\pi ic(\nu-\nu_0)t]d\nu =\sum_n[(2\pi ict)^n/n!]M(n). \tag{27}$$

In the binary collision limit, Armstrong, Blumenfeld, and Gray[64] have written $\langle C^2\rangle$ in terms of an integral over the angular derivative of the interaction potential, $V(R,\theta)$:

$$\langle C^2\rangle=2\pi\rho\int\int[\partial V(R,\theta)/\partial\theta]^2 \times\exp[-V(R,\theta)K_BT]R^2\sin\theta\,d\theta\,dR, \tag{28}$$

where ρ is the number density of the perturbing gas, such as Ar in the CO_2–Ar system. We have calculated the mean square torque using Eq. (28) for the surfaces used here and compare them with the experimental results at room temperature[10] in Table II. PP1 gives the worst result. The *ab initio* and the Loesch potentials also yield $\langle C^2\rangle/\rho$ values that are much too large.

Steed, Dixon, and Klemperer used molecular beam electric resonance spectroscopy to measure spectroscopic and structural constants for the CO_2–Ar complex.[3] They also determined precisely the dipole moment of this complex from a measurement of the Stark effects on the rotational transitions. The equilibrium structure was observed to be T-shaped with an average separation of 3.493 Å between the Ar atom and the carbon atom in CO_2.[3] For this structure, a classical multipole calculation by Birnbaum[78] of the dipole induced in the Ar atom by the quadrupole of the CO_2 molecule yields $\mu=0.070$ D, based on the polarizability of Ar and the measured electric quadrupole moment of CO_2. This result agrees very well with the value reported by Steed, Dixon, and Klemperer, $\mu=0.06793$ D.[3] The harmonic force constants for the vdW stretching and bending k_s and k_b have been determined from the measured centrifugal distortion constants, and these in turn lead to estimates of the intermolecular stretching and bending harmonic frequencies, ω_s and $\omega_b=37.5$ and 38.9 cm^{-1}, respectively.[3,9] Recently, the ν_3 fundamental band of CO_2 and its combination band with the vdW bending have been reported for CO_2–Ar by Sharpe *et al.*, giving a more reliable value $\omega_b=27.8$ cm^{-1}.[6] We have obtained analytic first and second derivatives for each of the potentials, from which we calculated not only $\langle C^2\rangle/\rho$ as described above, but also the quadratic force constants for the stretch and bend of the CO_2–Ar complex. We calculated the intermolecular harmonic bending and stretching frequencies from these force constants using the standard FG matrix method.[79] We compare in Table II the predictions from the potential energy surfaces with the experimental data.[3,6] The poorest bending frequency comes from the Rotzoll–Lübbert potential. The 3A and the *ab initio* potentials also give too low bending frequencies, and PP1 yields too high a value. Nearly all potentials give a good accounting of the stretching force constant, except for PP1, which again yields a value too high.

The average rotational constants for the CO_2–Ar complex were reported by Steed, Dixon, and Klemperer[3] and Randall, Walsh, and Howard.[5] All the potential energy surfaces considered here involve the assumption that the CO_2 has the same geometry as the monomer and is a rigid entity. Our QDMC simulations on all of the potential surfaces yield the average structure, the average rotational constants for the ground vibrational state, and the average zero-point vibrational energy. The dissociation energy of the CO_2–Ar van der Waals complex (166 cm^{-1}) was determined by Bohac, Marshall, and Miller from the assignment of the final state distributions of the photofragments resulting from vibrational predissociation.[7] The average distance, rotational constants, and dissociation energy predicted by the various surfaces are compared with experimental values in Table III. The average intermolecular distance in the complex is longer than the $R_m(90°)$ of the potential by 0.06 to 0.18 Å. This is much larger than the zero-point vibrational corrections to most covalent bonds, of course. The rotational constants are in reasonably good agreement with experiment for most of the potential functions, with the BD potentials giving the worst results, followed by Loesch and PP2. The BD potential has much too long an $R_m(90°)$, leading to too small values of the B and C rotational constants. Loesch and PP2 potentials also have a bit too long $R_m(90°)$. The $\epsilon(90°)$ for the RL, PP2, and Loesch potentials are all smaller than the experimental dissociation energy of the complex. Thus it is not surprising that these PES give the smallest dissociation energies, less than 75% of the observed value. On the other hand, PP1 has too deep a global minimum, leading to a dissociation energy

TABLE II. Predictions of constants derived from spectroscopy of CO_2–Ar. Values (this work) with footnote indicators are in good agreement with the values from the work cited.

Observable	Expt.	Expt.	RL	PP1	PP2	3A	AD-M	3A-R	AD-R	Billing	Loesch	BD	*Ab initio*
k_s (mdyne/Å)	0.0174 (Ref. 3)	0.017 38 (Ref. 4)	0.016 16	0.0397[a]	0.0152[d]	0.026 42[g]	0.0266	0.013 93	0.013 53	0.021 336	0.013 94[o]	0.016 15	0.023 23
k_b (mdyne Å)	0.0083 (Ref. 3)	0.009 428 (Ref. 4)	0.000 375	0.0288[b]	0.0028[e]	0.000 790[h]	0.003 55	0.009 42	0.009 696	0.003 288	0.009 42[p]	0.009 32	0.001 18
ω_s (cm^{-1})	37.5 (Ref. 3)	37.5 (Ref. 4)	36.1	56.5	35.0	46.1[i]	46.3	33.6[l]	33.1[n]	33.1	33.6[q]	36.1	43.3
ω_b (cm^{-1})	27.5 (Ref. 3)	29.4 (Ref. 4) 27.8 (Ref. 6)	5.9	52.0	15.9	8.5[j]	18.1[k]	29.5[m]	29.9[m]	16.9	29.3[r]	28.8	10.4
$\langle C^2\rangle/\rho$ (cm^{-2}/amagat)	690 (Ref. 10)		960	2750[c]	1150[f]	1330	1270	590	540	780	1890	580	1970

[a]0.038 mdyn/Å from Steed, Dixon, and Klemperer (Ref. 3).
[b]0.028 mdyne Å from Steed, Dixon, and Klemperer (Ref. 3).
[c]2800 cm^{-2}/amagat from Dreyfus, Berreby, and Dayan (Ref. 10).
[d]0.0154 mdyne/Å from Dreyfus, Berreby, and Dayan (Ref. 10).
[e]0.0029 mdyne Å from Dreyfus, Berreby, and Dayan (Ref. 10).
[f]950 cm^{-2}/amagat from Dreyfus, Berreby, and Dayan (Ref. 10).
[g]0.0263 mdyne/Å from Fraser, Pine, and Suenram (Ref. 4).
[h]0.000 786 mdyne Å from Fraser, Pine, and Suenran (Ref. 4).
[i]46.1 cm^{-1}, 44.8 cm^{-1} (anharmonic) from Fraser, Pine, and Suenram (Ref. 4).
[j]8.5 cm^{-1}, 18.3 cm^{-1} (anharmonic) from Fraser, Pine, and Suenram (Ref. 4), 18.3 cm^{-1} (anharmonic) from Bohac, Marshall, and Miller (Ref. 7).
[k]17.9 cm^{-1} (anharmonic) from Bohac, Marshall, and Miller (Ref. 7).
[l]30 cm^{-1} (anharmonic) from Bohac, Marshall, and Miller (Ref. 7).
[m]Both the AD-R and the 3A-R potentials were fit by Bohac, Marshall, and Miller (Ref. 7) to 27.8 cm^{-1} (anharmonic).
[n]29 cm^{-1} (anharmonic) from Bohac, Marshall, and Miller (Ref. 7).
[o]0.0140 mdyn/Å from Steed, Dixon, and Klemperer (Ref. 3).
[p]0.0094 mdyn Å from Steed, Dixon, and Klemperer (Ref. 3).
[q]33.6 cm^{-1} from Steed, Dixon, and Klemperer (Ref. 3).
[r]29.4 cm^{-1} from Steed, Dixon, and Klemperer (Ref. 3).

TABLE III. Comparison of spectroscopic data predicted by QDMC averaging on various surfaces.

Observable	Expt.	Expt.[a] (Ref. 4)	RL	PP1	PP2	3A	AD-M	3A-R	AD-R	Billing	Loesch	BD	*Ab initio*
$\langle R_m \rangle$ (Å)	3.493 ±0.010 (Ref. 3)	3.5048 ±0.0001 (Ref. 4)	3.5976	3.3521	3.7289	3.5178	3.5232	3.5158	3.5206	3.6169	3.7566	4.0404	3.5650
A (MHz)	11 914 ±80 (Ref. 3)	11953.3 ±9.2 (Ref. 4)	13467.8 ±40.9	11850.5 ±3.5	13254.8 ±39.6	12049.3 ±3.0	12140.6 ±6.1	11959.5 ±3.4	11953.3 ±2.9	12174.0 ±6.6	11987.5 ±4.96	11973.9 ±3.1	12048.9 ±4.6
B (MHz)	1979.87 ±0.25 (Ref. 3)	1979.943 ±0.050 (Ref. 4)	1856.9 ±2.1	2153.3 ±3.1	1735.4 ±1.0	1951.4 ±1.5	1943.6 ±1.2	1958.6 ±1.3	1954.3 ±1.6	1844.9 ±1.8	1716.0 ±2.4	1481.7 ±0.9	1900.8 ±1.5
C (MHz)	1682.75 ±0.20 (Ref. 3)	1682.237 ±0.052 (Ref. 4)	1619.1 ±1.4	1820.6 ±2.2	1521.6 ±0.7	1677.6 ±1.1	1673.2 ±0.8	1681.0 ±0.9	1677.6 ±1.2	1599.8 ±1.3	1499.3 ±1.8	1317.5 ±0.7	1639.9 ±1.2
D_0 (cm^{-1})	166 ±1 (Ref. 7)		111.7 ±0.2	228.1 ±0.1	120.7 ±0.7	171.8 ±0.2	156.0 ±0.1	166.1 was fitted (Ref. 7)	165.9 ±0.2	148.0 ±0.6	125.9 ±0.4	145.1 ±0.2	180.2 ±0.2
						171.9 (Ref. 4)			was fitted (Ref. 7)				

[a]Rotational constants $A=11\,904.36\pm0.91$, $B=1978.979\pm0.097$, $C=1683.12\pm0.11$ MHz were reported by Ref. 5 at the same time as Ref. 4.

1.4 times that observed. The potentials are all anharmonic, with zero-point energies all very close to 30 cm^{-1}, except for RL and PP2, which are smaller, and PP1, which gives 50.6 cm^{-1}.

C. Classical trajectory results for various CO_2–Ar surfaces

The following surfaces were chosen for trajectory studies: the *ab initio* surface of Marshall *et al.*,[30] the Rotzoll–Lübbert surface (RL),[24] surfaces 1 (PP1) and 2 (PP2) from Pack and co-workers,[2,23] Hough and Howard's three-angle parametrized $(n-6)$ surface (3A) and their angle-dependent surface with m allowed to vary (AD-M).[28] The Rotzoll and Lübbert surface (instead of the Loesch surface) was chosen to allow comparison of a simple LJ(12,6) surface with the more complex surfaces. Rotzoll has also proposed a N_2–Kr surface using the same approach, and it has proven to be a useful surface despite its simple form.[40,41]

1. Transport properties

Although the classical trajectories yield 48 different cross sections, experimental data exist for comparison of only a few cross sections, those that are involved in the diffusion coefficient, mixture viscosity, and thermal conductivity for the CO_2–Ar system. Within the first-order Chapman–Cowling approximation[33] of a binary mixture of components A and B, the binary diffusion coefficient is given by[31]

$$D_{AB}=k_BT/[m_A\rho_AL_0\langle v\rangle\sigma(1000|A)_{AB}]. \tag{29}$$

L_0 is Loschmidt's number ($2.686\,763\times10^{25}$ molecules m^{-3}), $\langle v\rangle$ is the mean relative velocity, and ρ_A is the density of A in amagats. A number of values for the CO_2–Ar diffusion coefficient have been reported.[19–22] These values are plotted against the predictions of six surfaces in Fig. 4. The cross sections involved in the mixture viscosity $\eta_{\rm mix}$,[31,80] i.e., $\sigma(2000|A)_{AA}$, $\sigma(2000|B)_{BB}$, $\sigma(2000|A)_{AB}$, $\sigma(2000|B)_{AB}$, and the transfer cross section

$$\sigma\begin{pmatrix}2&0&0&0&A\\2&0&0&0&B\end{pmatrix}_{AB},$$

do not involve angular momentum changes and are not very sensitive to the anisotropy of the potential surface. The viscosity data of Refs. 16 and 17 are plotted with the results of the trajectory calculations in Fig. 5. The calculated values have been effectively scaled to the pure CO_2 and Ar experimental data since the pure gas cross sections are needed in the calculation of $\eta_{\rm mix}$. The experimental viscosity data show a linear dependence on the CO_2 mole fraction x_{CO_2} at room temperature. As 873 K is approached, curvature brings the mole fraction dependence slightly below a linear dependence at $x_{CO_2}\sim0.5$.

In contrast to the diffusion and viscosity, the thermal conductivity has a contribution from the molecular angular momentum of the rotor. Within the first-order Chapman–Cowling expression, the thermal conductivity coefficient depends on the cross sections $\sigma(1001|A)_{AB}$, $\sigma(1010|A)_{AB}$, and $\sigma(1010|B)_{AB}$, as well as the pure gas cross sections

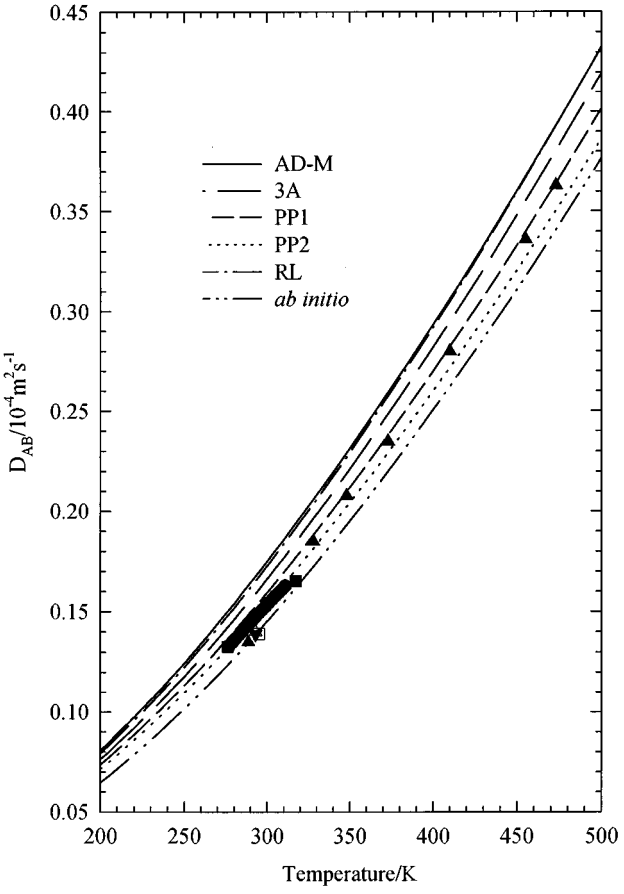

FIG. 4. Temperature dependence of the diffusion coefficient in CO_2–Ar calculated using various surfaces compared with experiment: ●, Robjohns and Dunlop (Ref. 22); ■, Holsen and Strunk (Ref. 19); ▲, Ivankin and Suetin (Ref. 20); ▼, Waldman, Ref. 24 in Pakurar and Ferron (Ref. 21); □, Pakurar and Ferro, Ref. 21 in Pakurar and Ferron (Ref. 21); △, Ref. 1 in Pakurar and Ferron (Ref. 21).

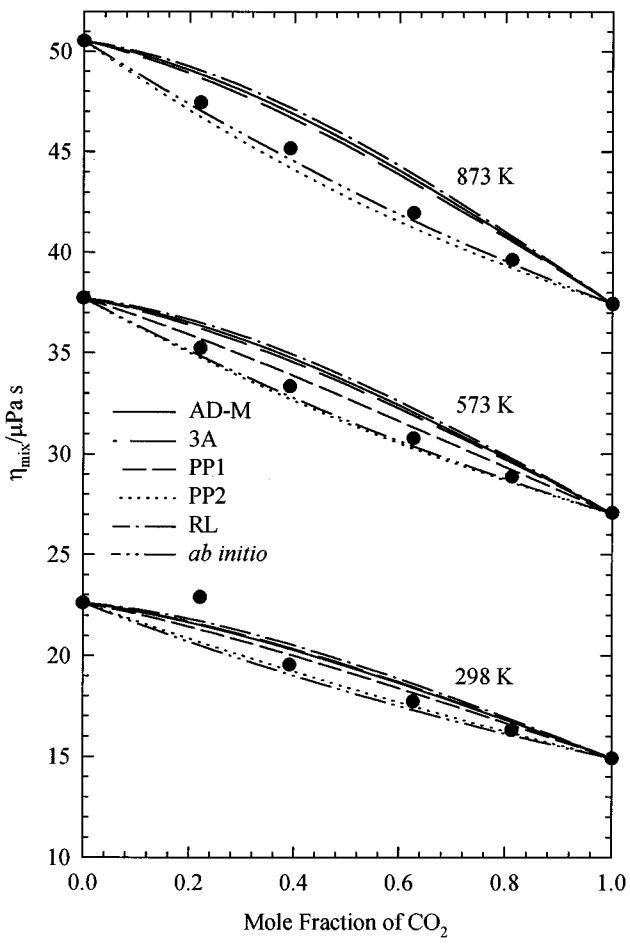

FIG. 5. Mole-fraction dependence of the mixture viscosity in CO_2–Ar calculated using six surfaces at three temperatures, experimental data from Kestin and co-workers (Refs. 16 and 17).

$\sigma(1010|B)_{BB}$, for the rare gas and $\sigma(1010|A)_{AA}$ and $\sigma(1001|A)_{AA}$ for CO_2.[81] Here, too, only the mole-fraction dependence of the thermal conductivity coefficient can be compared with experiment. Because the masses of Ar and CO_2 are close, the effects which normally dominate the composition dependence of the thermal conductivity are small so that the effects arising from inelastic collisions should be observable. Furthermore, the thermal conductivities of the pure components differ by only 6%. In Fig. 6, we compare the observed composition dependence of the thermal conductivity in CO_2–Ar mixtures[18] with those calculated from the cross sections.

2. NMR cross sections

In the density regime where the frequency of collisions exceeds the nuclear Larmor frequency (the so-called extreme narrowing limit), the spin–lattice relaxation time T_1 has a linear dependence on density ρ. When the spin relaxation is completely dominated by a single mechanism such as the spin-rotation mechanism, then measurements of T_1/ρ as a function of temperature for the pure gas establishes the characteristics of the like-molecule collisions. It has been shown experimentally and theoretically that in the extreme narrowing limit the spin-rotation (or the quadrupolar) relaxation time in a mixture is made up of additive contributions from various collision partners, provided the gas pressures are low enough such that the effects of successive collisions are not correlated:[82]

$$T_1=(T_1/\rho)_{AA}\rho_A+(T_1/\rho)_{AB}\rho_B. \tag{30}$$

In the CO_2–Ar system the spin relaxation of the ^{13}C in the gas phase is dominated entirely by the spin-rotation mechanism so the values of $(T_1/\rho)_{\mathrm{lin},CO_2\text{-}Ar}$ can be related directly to the cross section $\sigma(0100|A)_{AB}$ through the spin-rotation coupling constant C_{eff}, which involves components of the spin-rotation coupling tensor. For a linear molecule C_{eff} is the perpendicular component of the spin-rotation tensor, and the relation between the relaxation time and the cross section is

$$T_1=(3\hbar^2/2C_{\mathrm{eff}}^2 I_0 k_B T)\rho\langle v\rangle\sigma(0100|A)_{AB}. \tag{31}$$

The cross section $\sigma(0100|A)_{AB}$ is also known as σ_J. The spin rotation constant for the $^{13}CO_2$ molecule has been measured.[83] Thus, it is possible to determine $\sigma(0100|A)_{AB}$

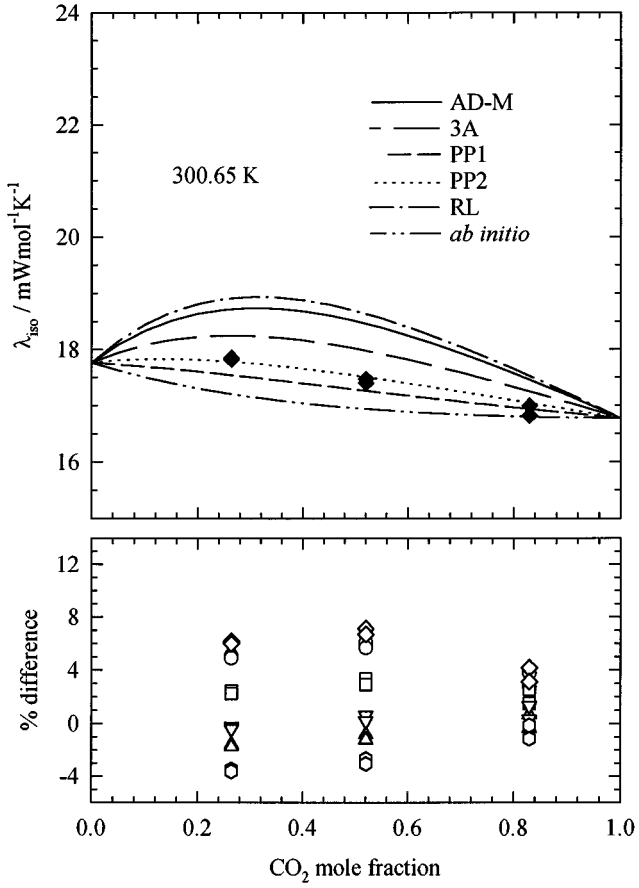

FIG. 6. Mole-fraction dependence of the thermal conductivity coefficient in CO_2–Ar calculated using six surfaces, experimental data from Kestin, Nagasaka, and Wakeham (Ref. 18). Percent differences are shown in the bottom frame for the same surfaces: ○, AD-M; □, 3A; △, PP1; ▽, PP2; ◇, RL; hexagons, *ab initio*.

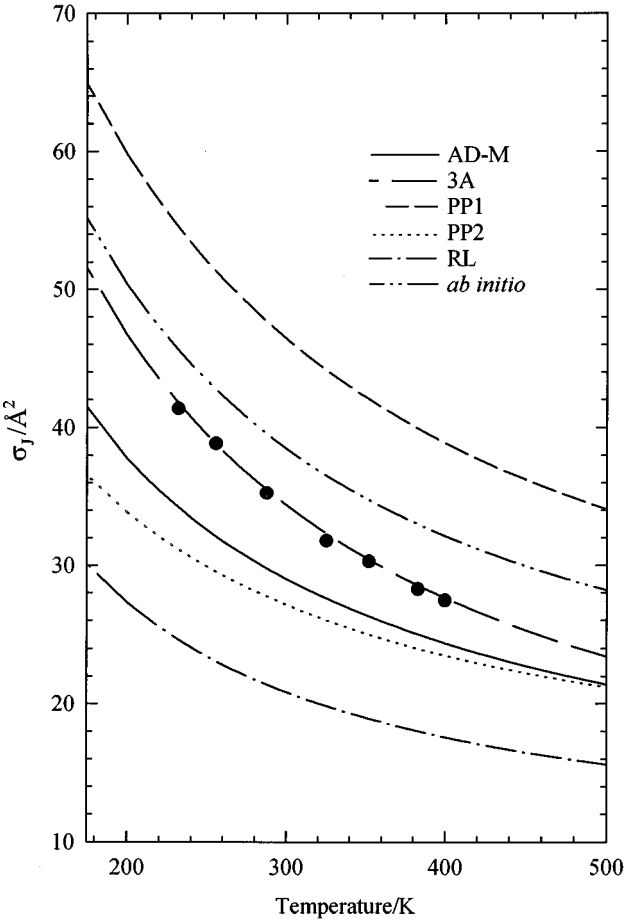

FIG. 7. Temperature dependence of σ_J in CO_2–Ar calculated using six surfaces compared with experimental data of Jameson *et al.* (Ref. 84).

for the CO_2–Ar system directly from spin relaxation experiments in the mixture. The ^{13}C relaxation measurements in the gas phase in mixtures of CO_2 and Ar have been done in our laboratory and reported earlier.[84] In these studies it had been found that $(T_1/\rho)_{\mathrm{lin},CO_2\text{-}CO_2}$ had a $T^{-1.5}$ dependence, but the measurements in the pure CO_2 gas were limited to temperatures above 290 K. It has since been demonstrated that the temperature dependence of the pure CO_2 relaxation is $T^{-1.5}$ even into the dense phase region where T_1 is no longer a linear function of the density.[85] If we extrapolate the pure CO_2 data down to 220 K with this temperature dependence, the measurements in CO_2–Ar mixtures then provide $(T_1/\rho)_{\mathrm{lin},CO_2\text{-}Ar}$ that are valid in the range 220–400 K. Since the σ_J values were experimentally determined from spin relaxation of spin-1/2 ^{13}C nuclei in CO_2–Ar mixtures, the mass of $^{13}CO_2$ was used in the trajectories. The diffusion and viscosity data were taken from natural abundance CO_2, however. The difference in the mass of $^{12}CO_2$ and $^{13}CO_2$ is not expected to affect the trajectory results to a great degree. To verify this, a set of trajectories was run for $^{12}CO_2$. The two sets of cross sections generally do not differ by more than the estimated uncertainty in the various cross sections. The values of σ_J calculated from the six surfaces are shown in Fig. 7.

Although experimental values for the other NMR relaxation cross section $\sigma_{\theta,2}=\sigma(0200|A)_{AB}$ are not presently available for the CO_2–Ar system, comparison of this cross section among the surfaces is made in Fig. 8. This cross section is the same as the depolarized Rayleigh scattering cross section σ_{DPR} in the case of CO_2–Ar since the collision partner Ar has no rotational degrees of freedom to contribute. The only experimental indication of the magnitude of $\sigma_{\theta,2}$ for the CO_2–Ar system can be obtained from depolarized Rayleigh light scattering experiments on the CO_2–CO_2 system. If we assume that the contribution to σ_{DPR} from the other CO_2 molecule is small so that $\sigma_{\mathrm{DPR}}\sim\sigma_{\theta,2}$ and use the value of σ_J from the spin relaxation measurements in pure CO_2 gas,[84] then the ratio $\sigma_{\theta,2}/\sigma_J$ is 1.5 for the CO_2–CO_2 relaxation cross sections. Our previous experimental studies of these NMR cross sections[68,86] in the N_2–X and NNO–X systems show that $\sigma_{\theta,2}/\sigma_J$ is nearly constant and independent of the collision partner X. Assuming this relation,[68,86] $\sigma_{\theta,2}/\sigma_J$ is estimated to be 1.5 also for the CO_2–Ar system. Table IV shows the values of the cross section ratio at 300 K for each of the potentials.

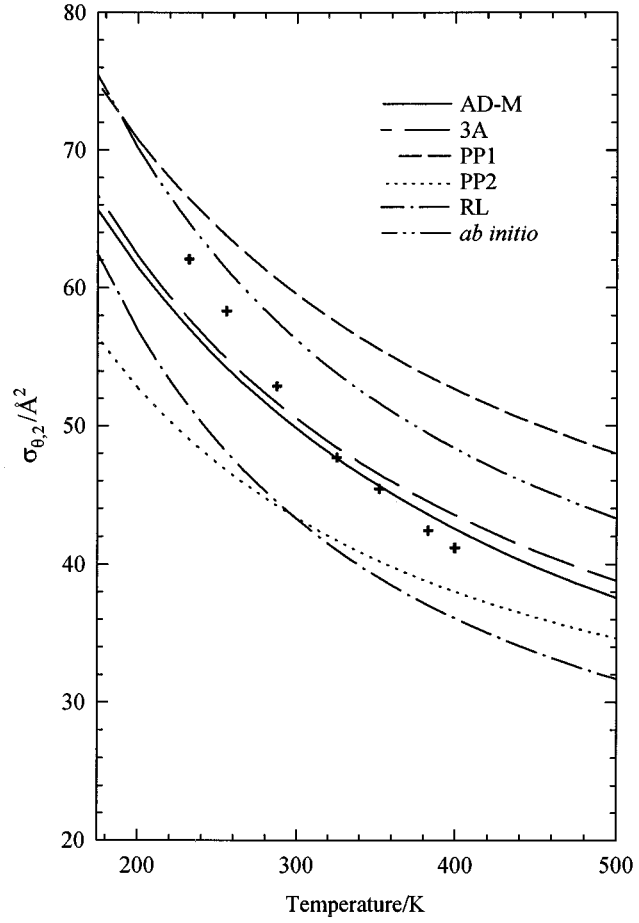

FIG. 8. Temperature dependence of $\sigma_{\theta,2}$ in CO_2–Ar calculated using six surfaces. Also shown (+) are the estimated values if the ratio $\sigma_{\theta,2}/\sigma_J$ is taken to be 1.5 as is found in CO_2–CO_2.

D. Close-coupling results

Initially, the classical trajectories at low total energies gave relatively poor agreement among some of the cross sections related by time-reversal symmetry. It was observed that an abnormally high number of trajectories were lost due to orbital resonance. That is, the CO_2 molecule and argon atom spent a long time experiencing the attractive region of the interaction potential surface. When this happened, the method used to integrate the equations of motion jumped out of this loop and discarded the results of the trajectory. We found later that we could greatly diminish the deviations from time-reversal symmetry by repeating the calculations on these surfaces using a larger set of orientation variables. Nonetheless, we carried out quantum CC scattering on one of the surfaces for comparison with the classical trajectory results to further study the effects of orbital resonances. The CC method does not break down with orbital resonances so that its predictions of cross sections from a PES provide an ''exact'' calculation by which the validity of the classical calculations can be assessed. However, since CO_2 has a small rotational constant (0.3902 cm^{-1}), many rotational states are populated even at 100 K; 90% of the molecules are in $j=0$ up to $j=19$. At the lowest total energy (40 cm^{-1}) used in the classical calculations, the greatest open j level is $j=8$ but the total symmetry of the wave function restricts population to only the even j states.

The 3A surface was used to calculate the S-matrix elements at a total energy of 40 cm^{-1}. Each energy-dependent cross sections $\sigma_\alpha[E]$ is formed from a summation over j-weighted state-to-state effective cross section $\sigma_\alpha(j'j)$ where j is the initial rotational state and j' is the final state. It is these j-dependent cross sections that are directly calculated from the S-matrix elements. For example, the expressions for σ_{DPR} are as follows. The thermal average cross section is

$$\sigma_{\mathrm{DRP}}(T)=(Z_{\mathrm{rot}}N_{\mathrm{DPR}})^{-1}\int dX\ \exp(-X)X\sigma_{\mathrm{DPR}}[E], \tag{32}$$

where Z_{rot} is the rotational partition function $[\Sigma_j(2j+1)\exp(-E_j/k_BT)]$ and

$$N_{\mathrm{DPR}}=\sum_j \rho_j d_j^2, \quad \rho_j=\exp(-E_j/k_BT)/Z_{\mathrm{rot}}. \tag{33}$$

The reduced matrix element of the angular momentum polarization, $\underline{d}_j$, is given by

$$\underline{d}_j=d_j/[j(j+1)-3/4] \tag{34}$$

and

$$d_j=\{(1/6)(2j+1)j(j+1)[4j(j+1)-3]\}^{1/2}. \tag{35}$$

The integration element in Eq. (32) is $X=E_{\mathrm{tot}}/k_BT$. In terms of the state-to-state cross sections, the energy-dependent DPR cross section is

$$\sigma_{\mathrm{DPR}}[E]=\sum_{j'j}(1-E_j/E_{\mathrm{tot}})\underline{d}_{j'}\sigma_T(j'j)\underline{d}_j \tag{36}$$

TABLE IV. NMR cross sections calculated for the CO_2–Ar surfaces studied.

	RL	PP1	PP2	3A	AD-M	*Ab initio*
ΔR_m, Å anisotropy	1.14	1.66	1.02	1.46	1.55	1.23
$\Delta\sigma$, Å anisotropy	1.01	1.61	1.05	1.30	1.39	1.21
σ_J (300 K), Å^2	20.83	46.43	39.14	34.36	29.01	38.48
$\sigma_{\theta,2}$ (300 K), Å^2	43.25	59.53	59.82	50.52	49.81	56.24
$\sigma_{\theta,2}/\sigma_J$	2.08	1.28	1.53	1.47	1.72	1.46

TABLE V. Comparison of CC and CT results for the CO_2–Ar surface for $E=40$ cm^{-1}.

Cross section	CT[a] $\sigma_\alpha^{\rm cl}[E]$	CC[b] $\sigma_\alpha[E]$	Scaled CT[c] $\underline{\sigma}_\alpha[E]$	% diff.	Opacity functions Q_α
$\sigma_\eta^{(1)}$	5 408.12	2 669.00	2 704.06	1.31	$\langle 1-(E_{k'}/E_k)P_2(\mathbf{v}\cdot\mathbf{v}')\rangle$
$\sigma_\eta^{(2)}$	4 072.73	2 052.91	2 036.36	0.81	$(2/3)\langle 1-(E_{k'}/E_k)P_2(\mathbf{v}\cdot\mathbf{v}')\rangle$
	4 042.55		2 021.27	1.54	
$\sigma_{\rm DPR}$ or $\sigma_{\theta 2}$	5 560.36	2 775.75	2 768.14	0.27	$\langle 1-P_2(\mathbf{j}'\cdot\mathbf{j})\rangle$
$\sigma_{T\eta}$ or $\sigma(02\|20)$	5 355.53	2 424.90	2 677.77	10.4	$-\langle (E_{j'}/E_j)P_2(\mathbf{v}'\cdot\mathbf{j})\rangle$
$\sigma_{\eta T}$ or $\sigma(20\|02)$	5 011.80	2 424.90	2 505.90	3.34	$-\langle (E_{j'}/E_j)P_2(\mathbf{v}\cdot\mathbf{j}')\rangle$
σ_T or $\sigma(0200)$	10 842 700		5 421 350	7.89	
	10 697 200	5 024 700	5 348 600	6.45	$\langle 1-(E_{j'}/E_j)P_2(\mathbf{j}\cdot\mathbf{j}')\rangle$
	10 823 400		5 411 700	7.70	

[a]The classical energy-dependent cross sections are calculated using $\sigma[E]_\eta^{(1)\rm cl}=(E/8B)\{Q_{\eta 1},2,0\}$, $\sigma_\eta^{(2)\rm cl}[E]=(3E/32B)\{Q_{\eta 2},3,0\}$, $\sigma_{T\eta}{}^{\rm cl}[E]=(\sqrt{6}E^2/48B^2)\{Q_{T\eta},2,1\}$, $\sigma_{\eta T}{}^{\rm cl}[E]=(\sqrt{6}E^2/48B^2)\{Q_{\eta T},3,1\}$, and $\sigma_T{}^{\rm cl}[E]=(E^3/24B^3)\{Q_T,1,2\}$. The multiple values for $\sigma_{\eta 2}$ and σ_T use different functional forms for the opacities.

[b]The quantum mechanical energy-dependent cross sections are given by $\sigma_\eta^{(1)}[E]=\Sigma_{j'j}(1-E_{j'}/E_{\rm tot})^{1/2}\times\sigma_{\eta 1}(j,j')(1-E_{j'}/E_{\rm tot})^{3/2}$, $\sigma_\eta^{(2)}[E]=\Sigma_{j'j}(1-E_{j'}/E_{\rm tot})\sigma_{\eta 2}(j,j')(1-E_{j'}/E_{\rm tot})^2$, $\sigma_{T\eta}[E]=\Sigma_{j'j}(1-E_j/E_{\rm tot})^2\times\sigma_{T\eta}(j,j')d_{j'}$, $\sigma_{\eta T}[E]=\Sigma_{j'j}(1-E_j/E_{\rm tot})^2\sigma_{\eta T}(j',j)d_{j'}$, $\sigma_T[E]=\Sigma_{j'j}(1-E_j/E_{\rm tot})d_{j'}\sigma_T(j,'j)d_j$.

[c]Scaled classical cross sections have been calculated using $f_\alpha\sigma_\alpha[E]$ (see the text) where the f_α factors are all equal to 0.5000 except for $f_{\rm DPR}$, which is equal to 0.49783.

and the classical limit of Eq. (36) is

$$\sigma_{\rm DPR}^{\rm cl}[E]=(E_{\rm tot}/6B)\{Q_{\rm DPR},1,0\}, \tag{37}$$

where the curly bracket notation symbolizes the integration over rotational energies using the ω parameter:

$$\{G,n,m\}=\int (1-\omega)^n(1+\omega)^m G(\omega)d\omega \tag{38}$$

and

$$\omega=(E_r-E_k)/E_{\rm tot}, \tag{39}$$

where E_r is the initial rotational energy and the E_k is the initial translational (kinetic) energy. From the CC calculations on the 3A surface at a total energy of 40 cm^{-1}, the value for $\sigma_{\rm DPR}[E]$ determined from Eq. (36) is 2775.75. Using the same surface and $E_{\rm tot}$, the classical result calculated from Eq. (37) is 5560.36. Before the CC results are compared with the CT results, the classical result needs to be corrected since only even rotor states are actually populated whereas the classical calculations are oblivious to this. The correction is made by scaling the classical $\sigma_{\rm DPR}^{\rm cl}[E]$ by $(Z_{\rm rot}N_{\rm DPR})_{\rm even}/(Z_{\rm rot}N_{\rm DPR})_{\rm all}$, where the summation over the j states in $(Z_{\rm rot}N_{\rm DPR})_{\rm even}$ only includes the even j states. The scaled classical value is

$$\underline{\sigma}_{\rm DPR}[E]=f_{\rm DPR}\sigma_{\rm DPR}^{\rm cl}[E]=\frac{(Z_{\rm rot}N_{\rm DPR})_{\rm even}}{(Z_{\rm rot}N_{\rm DPR})_{\rm all}}\,\sigma_{\rm DPR}^{\rm cl}[E]. \tag{40}$$

The value of $f_{\rm DPR}$ is 0.497 83 for $j_{\rm max}=100$ and the scaled cross section $\underline{\sigma}_{\rm DPR}[E=40\ {\rm cm}^{-1}]$ is equal to 2768.14, which now can be compared directly with the CC result 2275.75. Of course, the thermal average over the scaled quantities is

$$\sigma_{\rm DPR}(T)=(Z_{\rm rot}N_{\rm DPR})_{\rm even}^{-1}\int dX\ \exp(-X)X\underline{\sigma}_{\rm DPR}[E], \tag{41}$$

so that the factor f_α once again puts the classical thermal average values back to the result obtained by ignoring symmetry altogether. For the other cross sections $f_\alpha=0.5000$.

Table V summarizes the values for the values from the CC calculations $\sigma_\alpha[40\ {\rm cm}^{-1}]$ and the scaled classical values $\underline{\sigma}_\alpha[40\ {\rm cm}^{-1}]$. In comparing the CC and CT results (columns 3 and 4 in Table V), we assume the differences are primarily related to errors in the CT results arising from lost trajectories due to orbital resonances.

V. DISCUSSION

Most of the surfaces agree reasonably well with the experimental mixed second virial coefficient over the entire temperature range. The Berreby and Dayan function, fitted to the mean square torque, could not reproduce the second virial coefficient, as seen in Fig. 3. The BD and *ab initio* surfaces give the poorest agreement with the virial coefficient. Likewise, the modified 3A-R and AD-R surfaces which had been fitted to the dissociation energy of the vdW complex and the bending frequency gave systematically poorer results for $B_{12}(T)$ at higher temperatures.

How accurate are our CT results? In the comparison against close-coupling calculations at 40 cm^{-1} in Table V, the greatest difference is in the $\sigma_{T\eta}$ cross section, which depends on the ratio of rotational energies $E_{j'}/E_j$ (common also to $\sigma_{\eta T}$) and depends on the angle between the initial and final angular momentum vectors. Since the CC vs CT difference in $\sigma_{\eta T}$ is smaller, the orbital resonances in the CT method appear to affect the final j more than the final velocity. Also, $\sigma_{\rm DPR}$ shows the best agreement between the two methods, further suggesting that changes in the magnitude of j are more affected by orbital resonances in the CT calculations than are reorientations of j. This explains the moderate discrepancy among the σ_T values. The agreement between $\sigma_\eta^{(1)}$ and $\sigma_\eta^{(2)}$ values implies that the misrepresentation of ve-

locity changes by the CT method is insignificant. Thus, for CO_2–Ar mixtures at very low temperatures one can expect classical values for the rotationally inelastic cross sections (such as σ_J) to have larger uncertainties than do those for the predominantly elastic cross sections.

As tests of potential surfaces, the mixture viscosity, the diffusion coefficient, and the thermal conductivity are not very discriminating, although some surfaces agree less well than others as shown in Figs. 4–6. The Billing surface was not included in the present CT calculations, but comparisons with the six surfaces used here can be made based on Billing's published results for the diffusion coefficient and the mixture viscosity.[26] The Billing surface does the best job at reproducing the experimental diffusion coefficient values, and both Pack surfaces PP1 and PP2 do very well too, as seen in Fig. 4. The temperature dependence predicted by the 3A surface matches the overall temperature dependence of the experimental data more closely than do the Pack surfaces. This difference is, however, relatively small. The 3A, AD-M, and RL surfaces all overestimate the experimental diffusion coefficients, although the 3A results fall near the experimental error bars. High temperature diffusion data would differentiate between these surfaces better. The mole-fraction dependence of the mixture viscosity gives rather similar results at room temperature for all 6 surfaces (Fig. 5). The PP2 surface reproduces the experimental values at 298 K and provides the best agreement at the higher temperatures. The other surfaces all predict values within the error bars at 298 K but become progressively worse at the higher temperatures. The Billing surface shows the worst agreement at the high temperatures. Only two of the surfaces (the PP2 and *ab initio* surfaces) predict the concave nature of the mole-fraction dependence exhibited by the high temperature experimental data. The thermal conductivity is even less discriminating, with most surfaces giving within $\pm 4\%$ error in comparison with experiment, since we only have data at one temperature and the thermal conductivities of the pure substances are fairly similar (Fig. 6). The RL and AD-M surfaces overestimate the deviations from an ideal mixture.

In the multiproperty analysis of the N_2–Ar potential energy surface, Beneventi *et al.* found the NMR cross sections $\sigma_{\theta,2}$ and σ_J to depend sensitively on the anisotropy in R_m (the radial position of the well) and also on the P_2 anisotropy in the repulsive wall.[39] In our previous analysis of the N_2–Kr system, we demonstrated the great sensitivity of the two NMR cross sections to the radial anisotropy just as was found in the N_2–Ar system[39] and also the sensitivity to the anisotropy of the well depth, which had never been noted before.[40] We find the anisotropies of the various surfaces for the CO_2–Ar system are discriminated by the NMR cross sections. The 3A surface appear to exactly reproduce the experimental data shown in Fig. 7. Since the error in the experimental values is about 1%, only the 3A surface agrees completely with experiment. The *ab initio* and AD-M surfaces also do reasonably well, whereas PP1 and RL are quite poor in predicting this cross section. The PP2 and RL surfaces both underestimate σ_J. It is interesting that the PP2 surface has similar radial anisotropy at the low repulsive wall as the RL surface yet yields larger σ_J values than the latter does. The same characteristics of the PP1 surface that lead to an extremely large mean square torque also lead it to overestimate σ_J.

Experimental investigations of σ_J in our laboratory have shown that the temperature dependence of the σ_J cross sections and also the relaxation times can be described by a power law over a 200 K temperature range,

$$\sigma_J(T) = \sigma_J(300\ \text{K})(T/300)^{m_J},$$

with $m_J < 0$.[87] We had found that the power law does indeed provide an adequate description of the NMR cross sections obtained from the CT results in the range 200–400 K for all the N_2–Kr PES studied, but that the value of the exponent m_J depends on the potential. (A more complex temperature dependence would be necessary to describe a much greater temperature range.) Likewise the CT results on the CO_2–Ar system demonstrate that the NMR cross sections are very sensitive to the details of the anisotropy of the PES. We find that the magnitudes, the temperature dependences and the ratio of the two NMR cross sections predicted by six different PES's are substantially different, with errors of up to $\pm 40\%$ in the magnitudes of σ_J. We had previously demonstrated with several different surfaces for the N_2–Kr system that the temperature dependences of the two NMR cross sections were not related.[40] That is, the temperature dependence of the NMR cross sections, not just their magnitudes, are sensitive tests of anisotropic potential surfaces. We find here that the predicted temperature dependences of the $\sigma_{\theta,2}$ and σ_J are different from each other for the six surfaces used.

Based on our empirical observations that the ratio of the two NMR cross sections are nearly independent of the collision partner,[68,86] we had predicted a $\sigma_{\theta,2}/\sigma_J$ ratio close to 1.5 for the CO_2–Ar system as well. Unfortunately there are no experimental results for $\sigma_{\theta,2}(T)$ or σ_{DPR} to compare with. However, the 3A PES, which gives excellent agreement with the experimental $\sigma_J(T)$, also give a $\sigma_{\theta,2}/\sigma_J$ ratio close to 1.5, the ratio that we found for the CO_2–CO_2 relaxation cross sections. So do the *ab initio* and PP2 surfaces. The worst predictions of σ_J (RL and PP1) also go hand in hand with ratios quite different from 1.5, which tends to support the extrapolation from the CO_2–CO_2 system. The 3A and AD-M surfaces give much more similar results for $\sigma_{\theta,2}$.

We compare the mean square torque obtained from the measurements of Berreby and Dayan[25] with the predictions of the various PES's of the integral in Eq. (28). We see that the Billing, AD-R, and 3A-R potential surfaces do as well as the BD potential that had been fitted to the mean square torque, while surface I of Preston and Pack gives a value that is a factor of 4 too large compared to experiment and the Loesch and *ab initio* surfaces yield values that are also too large. By its form, the mean square torque provides a good probe of the anisotropy of the entire surface. Indeed, Dreyfus, Berreby, and Dayan have shown that for the PP2 CO_2–Ar surface, the integrand of Eq. (28) varies with angle with the largest contributions from angles in the range $30° < \theta < 85°$ and R ranging from distances corresponding to the lower repulsive wall to just past the position of the well

minimum.[10] Whereas the other spectroscopic data provide information about the shape of the well at the global minimum, the mean square torque is determined to a large extent by the angle dependence of the potential energy in the region between the two extreme configurations. In the NNO–Ar and NNO–Kr systems we have found[68] that the mean square torque and the NMR cross section $\sigma_{\theta,2}$ probe nearly the same parts of the PES; the PES that had been fitted to the mean square torque is the one that reproduces the experimental $\sigma_{\theta,2}(T)$ data. The results for the CO_2–Ar system suggest that this may not be a general observation.

We examined the predictions by the various PES's of spectroscopic data for the van der Waals complex in terms of the force constants for intermolecular stretching and bending in the van der Waals complex, and the harmonic stretching and bending frequencies calculated from these using a Wilson FG matrix analysis.[79] The measured centrifugal distortion constants provide experimental values of the quadratic stretching and bending force constants for the complex[3] with which the predictions from the second derivatives of the various PES's were compared in Table II. It should be noted that we calculated only the harmonic frequencies. It has been shown that more accurate bending frequencies obtained by variational calculation using the 3A and 3A-M potentials are larger than the harmonic frequencies estimated from the quadratic force constants, whereas the stretching frequencies are quite close to harmonic. There is an observation by Sharpe *et al.*[6] of the bending frequency as a combination band with the asymmetric stretch of the CO_2 monomer, with which the predicted bending frequencies may be compared. These spectroscopic quantities are very sensitive to the shape of the well in the vicinity of the global minimum, from which we see in Table II that the 3A-R and the AD-R surfaces give the best descriptions. Surface I of Preston and Pack gives the worst stretching and bending force constants. The Rotzoll–Lübbert potential and the 3A potentials provide too small bending force constants. The average rotational constants are more sensitive to the absolute position of R_m and the softness of the radial anisotropy in the well region. We see in Table III that the Howard and Hough surfaces 3A, AD-M, including the modified ones 3A-R and AD-R, give the best average rotational constants and dissociation energy in the QDMC simulations. The *ab initio* surface also does well here. The dissociation energy is most sensitive to the shape of the well, not just the well depth at the global minimum. The *ab initio* surface gives reasonable agreement with the dissociation energy reported by Bohac, Marshall, and Miller.[7] The rotational constants are more discriminating than the dissociation energy in distinguishing the well regions of the various PES's, although the dissociation energy certainly tests the well depth at the global minimum. It is important, however, to have a PES that is fitted to more than the van der Waals spectroscopic data since these provide essentially no information on the high repulsive wall (as can be seen by the inability of those surfaces specifically modified to fit vdW data in reproducing the temperature dependence of the second virial coefficients).

Finally, a recent paper by Roche *et al.*[88] has come to our attention during the completion of the present work which considers in detail the ability of several of these PES's in predicting pressure broadening and the van der Waals spectra of the CO_2–Ar system. They carried out exact close-coupling calculations using seven different potentials and find that even the AD-R and 3A-R potentials, which had been fit to microwave line positions, do not reproduce the centrifugal distortion constants quantitatively. The only potential surface that gives a satisfactory account of the line broadening coefficients is the PP2 surface.

VI. CONCLUSIONS

We have examined the anisotropy of twelve potential surfaces that have been proposed for the CO_2–Ar system. The analytic derivatives in the vicinity of the global minima were used to predict the quadratic force constants for the stretching and bending of the vdW complex and compared with the experimental values deduced from spectroscopy. Wilson's FG matrix method was used to predict the harmonic stretching and bending frequencies. For each potential surface we calculated the interaction second virial coefficients as a function of temperature and the mean square torque and compared these with experimental data. We used a quantum diffusion Monte Carlo procedure to obtain the average rotational constants in the ground vibrational state and dissociation energy of the vdW complex that would be predicted by each surface. We compared these predictions with the values determined by radio frequency, microwave, and infrared spectroscopy. For six of the surfaces, we carried out classical trajectories to obtain the thermal average cross sections, from which we obtained diffusion coefficients D_{AB}, mixture viscosities η_{mix}, thermal conductivities λ_{iso}, and the NMR relaxation cross sections $\sigma_{\theta,2}$ and σ_J. We compared the calculated values for these properties with experimental data. By including a wide variety of observables, some very sensitive to the detailed shape of the well, others very sensitive to the anisotropy of the well depth, and others more sensitive to the anisotropy in the repulsive wall, we have tested most parts of the proposed surfaces.

Although the average zero-point energy does depend on the shape of the well, our QDMC calculations yield very nearly the same zero-point energy for the CO_2–Ar complex, for eight out of eleven surfaces. Thus, the dissociation energy gives the best estimate of the well depth at the global minimum: The $\epsilon(90°)$ of the PP1 surface is too large, while those of RL, PP2, and Loesch surfaces are too small. The 3A, AD-M and *ab initio* surfaces have about the right value of $\epsilon(90°)$. The 3A-R and the AD-R surfaces had been adjusted to reproduce the experimental dissociation energy, so the best estimate of $\epsilon(90°)$ is 196 cm^{-1}. The average rotational constants give the best estimate of the $R_m(90°)$. Although the shape of the well at the global minimum does affect the average geometry in the ground vibrational state, the PES's which have too small a value of $R_m(90°)$ result in too large values of B and C. Thus, we find that $R_m(90°)$ is too short in the PP1 surface and too long in the BD surface, also a bit long in the Loesch surface. The AD-R and 3A-R

surfaces were adjusted to reproduce the rotational constants. Thus, the best estimate of $R_m(90°)$ is just under 3.48 Å and very close to 3.450 Å. The bending frequency ω_b gives a good measure of the well width (at half depth, for example) in radians: The RL surface is too wide, so are the 3A and *ab initio* surfaces. On the other hand, PP1 is too narrow. The 3A-R and the AD-R global minimum bowl appears to have the right characteristics to reproduce all the spectroscopic constants, as should be since both were adjusted to do this. However, both have unrealistically too soft repulsive walls which would lead to poor values for thermophysical properties at high temperatures. For this reason we did not choose them to do the classical trajectory calculations of effective cross sections.

Finally, the spin-rotation relaxation cross section σ_J is excellently reproduced by the 3A surface, with the *ab initio* surface and AD-M surfaces giving a modestly good agreement with experiment. If we assume the ratio of these NMR relaxation cross sections to be the same as found in CO_2–CO_2 then the points drawn in Fig. 8 are estimates of the $\sigma_{\theta,2}$ for CO_2–Ar based on this ratio of 1.50. Unfortunately we do not have ^{17}O spin relaxation data in CO_2–Ar which would provide the $\sigma_{\theta,2}$ cross sections directly. But again the outliers are the same ones (RL and PP1) that resulted in great deviations from the experimental σ_J cross sections.

The mixed success of the various surfaces in reproducing the experimental data seems to indicate that not a single surface presently available can be considered the best potential surface for the CO_2–Ar system. The well region and its shape near the global minimum are adequately tested by the average molecular constants for the ground vibrational state. However, the overall anisotropy in the position of the minimum as well as the anisotropy in the well depth are sensitively probed by the NMR cross sections and the mean square torque, and no PES gives good agreement with these and also the spectroscopic constants. The thermal conductivity, mixture viscosity, interaction second virial coefficient, and mixture diffusion coefficients lend further support, although by themselves they do not discriminate among the PES's sufficiently to eliminate from contention the ones that are found to be in great disagreement with the spectroscopic data, the NMR cross sections, and the mean square torque. The PP1 surface gives probably the worst representation of the CO_2–Ar interaction, the global minimum is too deep, and the distance too short. The Billing surface is one of those which do not have gross disagreement with experimental data, but we unfortunately did not choose to do classical trajectories on this surface. The width (in ångstroms) of the well of the global minimum at half depth determines the ω_s (and the width in radians largely determines ω_b). It would appear that the well width at half depth (in ångstroms) is too narrow for the PP1, 3A, AD-M, and *ab initio* surfaces, while the width at half depth (in radians) is too wide for the RL, 3A, and *ab initio* surfaces and too narrow for PP1. Overall, the *ab initio* and 3A surfaces are not too bad. Of the empirical surfaces, the 3A surface gives the best overall agreement with experiments, which agrees with Hough and Howard's original assessment.[28] With the classical trajectory results, the 3A surface predicts both data that are determined by the shape of the well in the global minimum of the PES and the thermophysical properties which depend in a more general sense on the anisotropy of the whole surface. Although the modification of the 3A potential by Bohac, Marshall, and Miller gave excellent agreement with the spectroscopic properties that depend on the well region, the modifications considerably softened the repulsive wall and led to rather poor behavior of the predicted second virial coefficients at high temperatures. Although we have not done the classical trajectories with the modified surfaces, we expect the high temperature values of the thermophysical properties such as thermal conductivity, diffusion coefficient, and viscosity to deviate significantly from experiment. We verify once again how well the NMR cross sections differentiate among the various surfaces and provide a sensitive test of the radial anisotropy. Finally, the spectroscopic data provide excellent tests of the depth and shape of the well region, complementing the NMR cross sections and the mean square torque which probe the anisotropy of the surface more broadly.

Currently, the published fit to the *ab initio* surface of Marshall *et al.*[30] provides a disappointing representation of the PES. The fitting of the *ab initio* PES could be improved to better reproduce the second derivatives at the global minimum and improve agreement with the second virial coefficient. It already has reasonable agreement with the other observables. A second approach is to construct a piecewise PES such as the Morse–Morse–Spline–van der Waals (MMSV) form which has provided sufficient flexibility to give an excellent accounting of the N_2–Ar system, adjust it to the bowl of the best PES (3A-R or AD-R) to reproduce the spectroscopic constants. Fit the other regions to reproduce the mean square torque and the temperature dependence of the second virial coefficient; then do classical trajectories to predict σ_J and thermophysical properties to serve as independent tests.

ACKNOWLEDGMENTS

This research has been supported by the National Science Foundation (Grant No. CHE92-10790 and No. CHE95-28066). We are grateful to F. R. W. McCourt for encouraging us in this work and for enlightening discussions and to Clement Wong for his help in initiating the CO_2–Ar trajectory calculations. We thank Carey Bissonnette and F. R. W. McCourt for their hospitality and assistance in the close-coupling calculations carried out at University of Waterloo. We thank P. Sandler and V. Buch for a copy of their program QCLUSTER which we used in the diffusion Monte Carlo calculations. We are grateful to A. Dickinson for permission to use his classical trajectory code.

APPENDIX

Lists of calculated effective cross sections for the various CO_2–Ar surfaces are presented in Tables VI A–VI F.

TABLE VI. (A) Selected effective cross sections calculated from the AD-M surface.[a] (B) Selected effective cross sections calculated from the 3A surface.[b] (C) Selected effective cross sections calculated from the PP1 surface.[c] (D) Selected effective cross sections calculated from the PP2 surface.[d] (E) Selected effective cross sections calculated from the RL surface.[e] (F) Selected effective cross sections calculated from the *ab initio* surface.[f] All cross sections are in units of Å^2.

	100 K	300 K	500 K	800 K
(A)				
$\sigma\eta^{(1)}$	44.661	25.048	21.832	19.921
$\sigma\theta_{,2}$	85.321	49.806	37.563	29.341
σ_J	61.296	29.010	21.404	16.470
$\sigma(2000\|A)_{AB}$	72.309	41.459	35.755	32.484
$\sigma\left(\begin{matrix}1\,0\,1\,0\|A\\1\,0\,0\,1\|A\end{matrix}\right)_{AB}$	−14.347	−8.070	−5.877	−4.499
$\sigma(1010\|A)_{AB}$	70.765	41.538	35.249	31.615
$\sigma(1010\|B)_{AB}$	72.663	42.362	36.525	32.918
$\sigma\left(\begin{matrix}1\,01\,0\|A\\1\,01\,0\|B\end{matrix}\right)_{AB}$	−18.356	−10.363	−9.902	−9.481
$\sigma\left(\begin{matrix}1\,0\,0\,1\|A\\1\,0\,1\,0\|B\end{matrix}\right)_{AB}$	−18.103	−13.297	−9.550	−7.507
$\sigma(1001\|A)_{AB}$	72.370	42.904	34.826	29.620
$\sigma(0001\|A)_{AB}$	43.399	24.476	19.137	15.283
$\sigma\eta^{(2)}$	27.852	16.515	13.947	12.567
$\sigma\left(\begin{matrix}2\,0\,0\,0\|A\\0\,2\,0\,0\|A\end{matrix}\right)_{AB}$	1.227	1.267	1.204	1.020
$\sigma(0200\|A)_{AB}$	77.108	40.990	29.427	22.440
$\sigma_{SA}(1200\|A)_{AB}$	92.229	52.088	40.732	33.766
$\sigma_{SA}(1100\|A)_{AB}$	83.135	43.701	34.892	29.465
$\sigma\left(\begin{matrix}1\,0\,0\,0\|A\\1\,2\,0\,0\|A\end{matrix}\right)_{AB}$	−3.107	−2.365	−1.829	−1.539
$\sigma\left(\begin{matrix}1\,0\,1\,0\|A\\1\,2\,0\,0\|A\end{matrix}\right)_{AB}$	−0.897	−1.043	−.743	−0.590
$\sigma\left(\begin{matrix}1\,0\,0\,1\|A\\1\,2\,0\,0\|A\end{matrix}\right)_{AB}$	10.847	8.245	6.835	5.830
$\sigma\left(\begin{matrix}1\,0\,0\,0\|A\\1\,1\,0\,0\|A\end{matrix}\right)_{AB}$	3.318	0.751	0.032	−0.253
$\sigma\left(\begin{matrix}1\,0\,1\,0\|A\\1\,1\,0\,0\|A\end{matrix}\right)_{AB}$	−0.697	0.186	0.169	0.130
$\sigma\left(\begin{matrix}1\,0\,0\,1\|A\\1\,1\,0\,0\|A\end{matrix}\right)_{AB}$	0.523	0.582	0.329	0.172
(B)				
$\sigma\eta^{(1)}$	45.933	26.328	22.475	20.210
$\sigma\theta_{,2}$	87.579	50.524	38.808	30.741
σ_J	75.027	34.359	23.403	16.741
$\sigma(2000\|A)_{AB}$	72.573	42.357	36.220	32.620
$\sigma\left(\begin{matrix}1\,0\,1\,0\|A\\1\,0\,0\,1\|A\end{matrix}\right)_{AB}$	−13.598	−7.248	−5.357	−4.080
$\sigma(1010\|A)_{AB}$	70.890	41.898	35.531	31.659
$\sigma(1010\|B)_{AB}$	74.000	44.127	37.450	33.343
$\sigma\left(\begin{matrix}1\,0\,1\,0\|A\\1\,0\,1\,0\|B\end{matrix}\right)_{AB}$	−20.766	−12.193	−10.702	−9.840
$\sigma\left(\begin{matrix}1\,0\,0\,1\|A\\1\,0\,1\,0\|B\end{matrix}\right)_{AB}$	−15.976	−10.778	−8.580	−6.930
$\sigma(1001\|A)_{AB}$	72.170	42.282	34.058	28.714
$\sigma(0001\|A)_{AB}$	41.050	23.801	18.162	14.165
$\sigma\eta^{(2)}$	26.644	16.031	13.746	12.410
$\sigma\left(\begin{matrix}2\,0\,0\,0\|A\\0\,2\,0\,0\|A\end{matrix}\right)_{AB}$	1.816	1.469	1.198	0.953
$\sigma(0200\|A)_{AB}$	81.576	41.898	29.684	21.818
$\sigma_{SA}(1200\|A)_{AB}$	97.219	52.917	40.742	33.133
$\sigma_{SA}(1100\|A)_{AB}$	92.016	47.063	36.084	29.524
$\sigma\left(\begin{matrix}1\,0\,0\,0\|A\\1\,2\,0\,0\|A\end{matrix}\right)_{AB}$	−2.296	−2.189	−1.866	−1.602
$\sigma\left(\begin{matrix}1\,0\,1\,0\|A\\1\,2\,0\,0\|A\end{matrix}\right)_{AB}$	−0.185	−0.689	−0.651	−0.568
$\sigma\left(\begin{matrix}1\,0\,0\,1\|A\\1\,2\,0\,0\|A\end{matrix}\right)_{AB}$	8.737	7.989	6.834	5.758
$\sigma\left(\begin{matrix}1\,0\,0\,0\|A\\1\,1\,0\,0\|A\end{matrix}\right)_{AB}$	1.484	0.102	−0.248	−0.367
$\sigma\left(\begin{matrix}1\,0\,1\,0\|A\\1\,1\,0\,0\|A\end{matrix}\right)_{AB}$	−0.368	0.280	0.242	0.189
$\sigma\left(\begin{matrix}1\,0\,0\,1\|A\\1\,1\,0\,0\|A\end{matrix}\right)_{AB}$	0.782	−0.078	−0.145	−0.155
(C)				
$\sigma\eta^{(1)}$	46.096	27.447	23.485	21.130
$\sigma\theta_{,2}$	93.779	59.530	47.968	39.759
σ_J	88.825	46.427	34.055	26.287
$\sigma(2000\|A)_{AB}$	73.062	44.084	37.802	34.104
$\sigma\left(\begin{matrix}1\,0\,1\,0\|A\\1\,0\,0\,1\|A\end{matrix}\right)_{AB}$	−14.843	−8.035	−6.308	−5.188
$\sigma(1010\|A)_{AB}$	71.908	43.724	37.334	33.443
$\sigma(1010\|B)_{AB}$	75.335	46.096	39.390	35.276
$\sigma\left(\begin{matrix}1\,0\,1\,0\|A\\1\,0\,1\,0\|B\end{matrix}\right)_{AB}$	−21.144	−13.143	−11.373	−10.251
$\sigma\left(\begin{matrix}1\,0\,0\,1\|A\\1\,0\,1\,0\|B\end{matrix}\right)_{AB}$	−13.960	−8.779	−7.563	−6.666
$\sigma(1001\|A)_{AB}$	75.537	45.505	37.787	32.765
$\sigma(0001\|A)_{AB}$	42.229	23.853	19.312	16.275
$\sigma\eta^{(2)}$	26.969	16.637	14.317	12.974
$\sigma\left(\begin{matrix}2\,0\,0\,0\|A\\0\,2\,0\,0\|A\end{matrix}\right)_{AB}$	1.102	1.627	1.521	1.345
$\sigma(0200\|A)_{AB}$	93.168	52.517	39.714	31.369
$\sigma_{SA}(1200\|A)_{AB}$	105.400	61.374	48.619	40.494
$\sigma_{SA}(1100\|A)_{AB}$	101.120	55.436	43.376	35.990
$\sigma\left(\begin{matrix}1\,0\,0\,0\|A\\1\,2\,0\,0\|A\end{matrix}\right)_{AB}$	−0.306	−1.958	−1.937	−1.808
$\sigma\left(\begin{matrix}1\,0\,1\,0\|A\\1\,2\,0\,0\|A\end{matrix}\right)_{AB}$	0.130	−0.074	−0.211	−0.277
$\sigma\left(\begin{matrix}1\,0\,0\,1\|A\\1\,2\,0\,0\|A\end{matrix}\right)_{AB}$	5.435	6.739	6.522	6.096
$\sigma\left(\begin{matrix}1\,0\,0\,0\|A\\1\,1\,0\,0\|A\end{matrix}\right)_{AB}$	0.921	−0.486	−0.902	−1.063
$\sigma\left(\begin{matrix}1\,0\,1\,0\|A\\1\,1\,0\,0\|A\end{matrix}\right)_{AB}$	0.386	0.917	0.799	0.669
$\sigma\left(\begin{matrix}1\,0\,0\,1\|A\\1\,1\,0\,0\|A\end{matrix}\right)_{AB}$	−1.331	−1.508	−1.244	−1.020
(D)				
$\sigma\eta^{(1)}$	49.086	30.392	25.744	22.942
$\sigma\theta_{,2}$	75.811	46.569	37.368	31.168
σ_J	52.465	29.984	23.276	18.969
$\sigma(2000\|A)_{AB}$	78.487	49.518	41.731	37.191
$\sigma\left(\begin{matrix}1\,0\,1\,0\|A\\1\,0\,0\,1\|A\end{matrix}\right)_{AB}$	−18.662	−10.354	−7.368	−5.605

TABLE VI. (*Continued*.)

	100 K	300 K	500 K	800 K
$\sigma(1010\|A)_{AB}$	78.590	49.614	41.428	36.669
$\sigma(1010\|B)_{AB}$	82.266	−12.282	43.572	38.628
$\sigma\left(\begin{matrix}1\,0\,1\,0\|A\\1\,0\,1\,0\|B\end{matrix}\right)_{AB}$	−19.590	−16.807	−11.182	−10.511
$\sigma\left(\begin{matrix}1\,0\,0\,1\|A\\1\,0\,1\,0\|B\end{matrix}\right)_{AB}$	−25.262	47.692	−13.099	−10.650
$\sigma(1001\|A)_{AB}$	88.702	52.852	41.423	35.344
$\sigma(0001\|A)_{AB}$	58.978	34.860	25.757	20.211
$\sigma\eta^{(2)}$	29.411	19.129	15.989	14.249
$\sigma\left(\begin{matrix}2\,0\,0\,0\|A\\0\,2\,0\,0\|A\end{matrix}\right)_{AB}$	2.430	2.113	1.702	1.406
$\sigma(0200\|A)_{AB}$	70.668	40.821	31.222	25.475
$\sigma_{SA}(1200\|A)_{AB}$	94.522	55.366	43.837	37.625
$\sigma_{SA}(1100\|A)_{AB}$	80.801	47.348	38.117	32.726
$\sigma\left(\begin{matrix}1\,0\,0\,0\|A\\1\,2\,0\,0\|A\end{matrix}\right)_{AB}$	−0.945	−0.965	−1.038	−1.081
$\sigma\left(\begin{matrix}1\,0\,1\,0\|A\\1\,2\,0\,0\|A\end{matrix}\right)_{AB}$	−0.910	−0.772	−0.665	−0.617
$\sigma\left(\begin{matrix}1\,0\,0\,1\|A\\1\,2\,0\,0\|A\end{matrix}\right)_{AB}$	9.230	8.535	7.407	6.646
$\sigma\left(\begin{matrix}1\,0\,0\,0\|A\\1\,1\,0\,0\|A\end{matrix}\right)_{AB}$	2.405	0.262	−0.358	−0.657
$\sigma\left(\begin{matrix}1\,0\,1\,0\|A\\1\,1\,0\,0\|A\end{matrix}\right)_{AB}$	−0.507	0.207	0.308	0.318
$\sigma\left(\begin{matrix}1\,0\,0\,1\|A\\1\,1\,0\,0\|A\end{matrix}\right)_{AB}$	1.186	0.577	0.209	−0.002
(E)				
$\sigma\eta^{(1)}$	45.336	25.344	21.790	19.736
$\sigma\theta_{,2}$	91.136	43.248	31.681	24.995
σ_J	46.105	20.834	15.581	12.479
$\sigma(2000\|A)_{AB}$	72.467	41.062	35.217	31.866
$\sigma\left(\begin{matrix}1\,0\,1\,0\|A\\1\,0\,0\,1\|A\end{matrix}\right)_{AB}$	−16.419	−7.550	−5.352	−4.083
$\sigma(1010\|A)_{AB}$	72.051	40.947	34.705	31.067
$\sigma(1010\|B)_{AB}$	75.238	43.053	36.507	32.681
$\sigma\left(\begin{matrix}1\,0\,1\,0\|A\\1\,0\,1\,0\|B\end{matrix}\right)_{AB}$	−17.923	−10.842	−9.890	−9.304
$\sigma\left(\begin{matrix}1\,0\,0\,1\|A\\1\,0\,1\,0\|B\end{matrix}\right)_{AB}$	−23.627	−13.762	−10.536	−8.478
$\sigma(1001\|A)_{AB}$	80.314	41.683	33.112	28.161
$\sigma(0001\|A)_{AB}$	52.876	26.608	19.546	15.317
$\sigma\eta^{(2)}$	27.134	15.720	13.428	12.131
$\sigma\left(\begin{matrix}2\,0\,0\,0\|A\\0\,2\,0\,0\|A\end{matrix}\right)_{AB}$	2.457	1.674	1.303	1.054
$\sigma(0200\|A)_{AB}$	63.243	29.509	22.095	17.693
$\sigma_{SA}(1200\|A)_{AB}$	84.583	43.145	34.551	29.550
$\sigma_{SA}(1100\|A)_{AB}$	72.122	37.022	30.048	26.021
$\sigma\left(\begin{matrix}1\,0\,0\,0\|A\\1\,2\,0\,0\|A\end{matrix}\right)_{AB}$	−0.792	−0.912	−0.920	−0.917
$\sigma\left(\begin{matrix}1\,0\,1\,0\|A\\1\,2\,0\,0\|A\end{matrix}\right)_{AB}$	−0.610	−0.683	−0.612	−0.540
$\sigma\left(\begin{matrix}1\,0\,0\,1\|A\\1\,2\,0\,0\|A\end{matrix}\right)_{AB}$	8.495	7.135	6.116	5.337
$\sigma\left(\begin{matrix}1\,0\,0\,0\|A\\1\,1\,0\,0\|A\end{matrix}\right)_{AB}$	2.593	0.377	−0.086	−0.276
$\sigma\left(\begin{matrix}1\,0\,1\,0\|A\\1\,1\,0\,0\|A\end{matrix}\right)_{AB}$	−0.578	0.060	0.079	0.079
$\sigma\left(\begin{matrix}1\,0\,0\,1\|A\\1\,1\,0\,0\|A\end{matrix}\right)_{AB}$	1.327	0.696	0.416	0.259
(F)				
$\sigma\eta^{(1)}$	56.304	30.144	25.035	22.236
$\sigma\theta_{,2}$	100.817	56.242	43.277	35.037
σ_J	78.890	38.484	28.187	22.070
$\sigma(2000\|A)_{AB}$	88.130	48.637	40.449	35.930
$\sigma\left(\begin{matrix}1\,0\,1\,0\|A\\1\,0\,0\,1\|A\end{matrix}\right)_{AB}$	−18.913	−10.087	−7.353	−5.679
$\sigma(1010\|A)_{AB}$	86.848	48.824	40.296	35.433
$\sigma(1010\|B)_{AB}$	75.238	51.371	42.437	37.292
$\sigma\left(\begin{matrix}1\,0\,1\,0\|A\\1\,0\,1\,0\|B\end{matrix}\right)_{AB}$	−17.923	−12.908	−11.180	−10.253
$\sigma\left(\begin{matrix}1\,0\,0\,1\|A\\1\,0\,1\,0\|B\end{matrix}\right)_{AB}$	−24.479	−15.373	−11.861	−9.576
$\sigma(1001\|A)_{AB}$	93.267	52.539	41.281	34.571
$\sigma(0001\|A)_{AB}$	58.751	33.226	24.805	19.482
$\sigma\eta^{(2)}$	31.833	18.494	15.414	13.692
$\sigma\left(\begin{matrix}2\,0\,0\,0\|A\\0\,2\,0\,0\|A\end{matrix}\right)_{AB}$	2.147	2.028	1.692	1.404
$\sigma(0200\|A)_{AB}$	91.848	47.920	35.668	28.177
$\sigma_{SA}(1200\|A)_{AB}$	112.948	60.132	46.758	38.885
$\sigma_{SA}(1100\|A)_{AB}$	103.744	52.665	40.884	34.164
$\sigma\left(\begin{matrix}1\,0\,0\,0\|A\\1\,2\,0\,0\|A\end{matrix}\right)_{AB}$	−1.981	−1.796	−1.605	−1.463
$\sigma\left(\begin{matrix}1\,0\,1\,0\|A\\1\,2\,0\,0\|A\end{matrix}\right)_{AB}$	−0.773	−0.718	−0.645	−0.572
$\sigma\left(\begin{matrix}1\,0\,0\,1\|A\\1\,2\,0\,0\|A\end{matrix}\right)_{AB}$	10.218	8.888	7.705	6.743
$\sigma\left(\begin{matrix}1\,0\,0\,0\|A\\1\,1\,0\,0\|A\end{matrix}\right)_{AB}$	2.538	0.068	−0.523	−0.780
$\sigma\left(\begin{matrix}1\,0\,1\,0\|A\\1\,1\,0\,0\|A\end{matrix}\right)_{AB}$	−0.640	0.376	0.406	0.380
$\sigma\left(\begin{matrix}1\,0\,0\,1\|A\\1\,1\,0\,0\|A\end{matrix}\right)_{AB}$	1.820	0.227	−0.050	−0.166

[a]Cross sections are for $^{12}CO_2$–Ar. Those related by time-reversal symmetry have been averaged over the pair and the average percent difference in these cross sections is greater than 50% at 100 K and about 2% at 800 K.
[b]Cross sections are for $^{13}CO_2$–Ar. Those related by time-reversal symmetry have been averaged over the pair and the average percent difference in these cross sections is 1% at 100 K and 0.3% at 800 K.
[c]Cross sections are for $^{13}CO_2$–Ar. Those related by time-reversal symmetry have been averaged over the pair and the average percent difference in these cross sections is 2% at 100 K and 0.1% at 800 K.
[d]Cross sections are for $^{13}CO_2$–Ar. Those related by time-reversal symmetry have been averaged over the pair and the average percent difference in these cross sections is 1% at 100 K and about 0.3% at 800 K.
[e]Cross sections are for $^{13}CO_2$–Ar. Those related by time-reversal symmetry have been averaged over the pair and the average percent difference in these cross sections is 1% at 100 K and 0.2% at 800 K.
[f]Cross sections are for $^{13}CO_2$–Ar. Those related by time reversal symmetry have been averaged over the pair and the average percent difference in these cross sections is about 1% at all four temperatures.

[1] H. J. Loesch, Chem. Phys. **18**, 431 (1976).
[2] G. A. Parker, R. L. Snow, and R. T Pack, J. Chem. Phys. **64**, 1668 (1976).
[3] J. M. Steed, T. A. Dixon, and W. Klemperer, J. Chem. Phys. **70**, 4095 (1979).
[4] G. T. Fraser, A. S. Pine, and R. D. Suenram, J. Chem. Phys. **88**, 6157 (1988).
[5] R. W. Randall, M. A. Walsh, and B. J. Howard, Faraday Discuss. Chem. Soc. (London) **85**, 13 (1988).
[6] S. W. Sharpe, D. Reifschneider, C. Wittig, and R. A. Beaudet, J. Chem. Phys. **94**, 233 (1991).
[7] E. J. Bohac, M. D. Marshall, and R. E. Miller, J. Chem. Phys. **97**, 4890 (1992).
[8] J. L. Fraites and D. H. Winicur, Mol. Phys. **35**, 927 (1978).
[9] C. H. Joyner, T. A. Dixon, F. A. Baiocchi, and W. Klemperer, J. Chem. Phys. **75**, 5285 (1981).
[10] C. Dreyfus, L. Berreby, and E. Dayan, Chem. Phys. Lett. **79**, 476 (1981).
[11] G. V. Andreeva, A. A. Kudryavtsev, M. V. Tonkov, and N. N. Filipov, Opt. Spectrosc. (USSR) **68**, 623 (1990).
[12] I. R. Dagg, A. Anderson, S. Yan, W. Smith, C. G. Joslin, and L. A. A. Read, Can. J. Phys. **64**, 1475 (1986).
[13] A. D. Afanasev, N. M. Grigorovich, and M. V. Tonkov, Opt. Spectrosc. (USSR) **58**, 772 (1985).
[14] T. L. Cottrell, R. A. Hamilton, and R. P. Taubinger, Trans. Faraday Soc. **52**, 1310 (1956).
[15] J. Brewer, *Determination of Mixed Virial Coefficients*, Technical Report No. AADD 663448, AFOSR No. 67-2795 (Air Force Office of Scientific Research, Arlington VA, 1967).
[16] J. Kestin, Y. Kobayashi, and R. T. Wood, Physica **32**, 1065 (1966).
[17] J. Kestin and S. T. Ro, Ber. Bunsenges, Phys. Chem. **78**, 20 (1974).
[18] J. Kestin, Y. Nagasaka, and W. A. Wakeham, Physica A **113**, 1 (1982).
[19] J. N. Holsen and M. R. Strunk, Ind. Eng. Chem. Fundam. **3**, 143 (1964).
[20] B. A. Ivanin and P. E. Suetin, Soviet Phys. Tech. Phys. **9**, 866 (1964).
[21] T. A. Pakurar and J. R. Ferron, Ind. Eng. Chem. Fundam. **5**, 533 (1966).
[22] H. L. Robjohns and P. J. Dunlop, Ber. Bunsenges. Phys. Chem. **88**, 1239 (1984).
[23] R. K. Preston and R. T Pack, J. Chem. Phys. **66**, 2480 (1977).
[24] G. Rotzoll and A. Lübbert, J. Chem. Phys. **71**, 2275 (1979).
[25] L. Berreby and E. Dayan, Mol. Phys. **48**, 581 (1983).
[26] G. D. Billing, Chem. Phys. **91**, 327 (1984).
[27] M. O. Bulanin, M. V. Tonkov, and N. N. Filipov, Can. J. Phys. **62**, 1306 (1984).
[28] A. M. Hough and B. J. Howard, J. Chem. Soc. Faraday Trans. 2 **83**, 191 (1987).
[29] M. Iida, Y. Ohshima, and Y. Endo, J. Phys. Chem. **97**, 357 (1993).
[30] P. J. Marshall, M. M. Szczesniak, G. Chalasinski, J. Sadlej, M. A. ter Horst, and C. J. Jameson, J. Chem. Phys. **104**, 6569 (1996).
[31] F. R. W. McCourt, J. J. M. Beenakker, W. E. Köhler, and I. Kuščer, *Nonequilibrium Phenomena in Polyatomic Gases*: *Vol. 1*, *The Dilute Gas* (Oxford University Press, Oxford, 1990).
[32] F. R. W. McCourt, J. J. M. Beenakker, W. E. Köhler, and I. Kuščer, *Nonequilibrium Phenomena in Polyatomic Gases*: *Vol. 2*, *Cross Sections, Scattering and Rarefied Gases* (Oxford University Press, Oxford, 1990).
[33] S. Chapman and T. G. Cowling, *Mathematical Theory of Non-Uniform Gases*, 3rd ed. (Cambridge University Press, Cambridge, 1970).
[34] C. F. Curtiss, J. Chem. Phys. **75**, 1341 (1981).
[35] C. F. Curtiss and M. W. Tonsager, J. Chem. Phys. **82**, 3795 (1985).
[36] A. S. Dickinson and M. S. Lee, J. Phys. B **18**, 3987 (1985).
[37] C. C. K. Wong, Ph.D. thesis, University of Waterloo, Waterloo, Ontario, Canada, 1991.
[38] L. Beneventi, P. Casavecchia, G. G. Volpi, C. C. K. Wong, and F. R. W. McCourt, J. Chem. Phys. **95**, 5827 (1991).
[39] L. Beneventi, P. Casavecchia, G. G. Volpi, C. C. K. Wong, and F. R. W. McCourt, J. Chem. Phys. **98**, 7926 (1993).
[40] M. A. ter Horst and C. J. Jameson, J. Chem. Phys. **102**, 4431 (1995).
[41] F. R. W. McCourt, M. A. ter Horst, and C. J. Jameson, J. Chem. Phys. **102**, 5752 (1995).
[42] A. S. Dickinson and M. S. Lee, J. Phys. B **19**, 3091 (1986).
[43] H. O'Hara and F. J. Smith, J. Comp. Phys. **5**, 328 (1970).
[44] A. M. Arthurs and A. Dalgarno, Proc. R. Soc. London Ser. A **256**, 540 (1960).
[45] H. Rabitz, J. Chem. Phys. **63**, 5208 (1975).
[46] MOLSCAT version 11, J. M. Hutson and S. Green, University of Durham, Durham, England, 1992.
[47] W. K. Liu, F. R. W. McCourt, and A. S. Dickinson, Mol. Phys. **66**, 565 (1989).
[48] J. B. Anderson J. Chem. Phys. **63**, 1499 (1975); **65**, 4121 (1976).
[49] V. Buch, J. Chem. Phys. **97**, 726 (1992).
[50] M. H. Kalos, Phys. Rev. A **2**, 250 (1970).
[51] B. J. Adler and D. M. Ceperley, J. Chem. Phys. **81**, 5833 (1984).
[52] M. A. Suhm and R. O. Watts, Phys. Rep. **204**, 293 (1991).
[53] G. C. Maitland, M. Rigby, E. B. Smith, and W. A. Wakeham, *Intermolecular Forces* (Clarendon, Oxford, 1981).
[54] R. A. Aziz, J. Chem. Phys. **65**, 490 (1976).
[55] A. Borysow and M. Moraldi, J. Chem. Phys. **99**, 8424 (1993).
[56] R. T Pack, J. Chem. Phys. **64**, 1659 (1976).
[57] E. A. Mason, private communications cited by Parker, Snow and Pack, Ref. 2.
[58] R. T Pack, J. Chem. Phys. **70**, 3424 (1979).
[59] R. T Pack, Chem. Phys. Lett. **55**, 197 (1978).
[60] A. D. Buckingham, Adv. Chem. Phys. **12**, 107 (1967).
[61] R. G. Gordon, J. Chem. Phys. **41**, 1819 (1964).
[62] C. Dreyfus (private communications cited by Billing, Ref. 26).
[63] A. M. Hough and B. J. Howard, J. Chem. Soc. Faraday Trans. 2 **83**, 173 (1987).
[64] R. L. Armstrong, J. M. Blumenfeld, and C. G. Gray, Can. J. Phys. **46**, 1331 (1968).
[65] R. J. Bemish, P. A. Block, L. G. Pedersen, W. Yang, and R. E. Miller, J. Chem. Phys. **99**, 8585 (1993).
[66] R. T Pack, J. Chem. Phys. **61**, 2091 (1974).
[67] C. Dreyfus, J. Mol. Liq. **43**, 241 (1989).
[68] M. A. ter Horst, Ph.D. thesis, University of Illinois at Chicago, 1993.
[69] R. T Pack, J. Chem. Phys. **78**, 7217 (1983).
[70] R. T Pack, Chem. Phys. Lett. **55**, 197 (1978).
[71] M. L. Martin, R. D. Trengove, K. R. Harris, and P. J. Dunlop, Aust. J. Chem. **35**, 1525 (1982).
[72] R. N. Lichtenthaler and K. Schafer, Ber. Bunsenges. Phys. Chem. **73**, 1525 (1969).
[73] H. Sutter and R. H. Cole, J. Chem. Phys. **52**, 140 (1970).
[74] B. Schramm, cited by J. H. Dymond and E. B. Smith, *The Virial Coefficients of Pure Gas Mixtures*. *A Critical Compilation* (Oxford University Press, Oxford, 1980).
[75] G. D. Billing (private communications).
[76] G. Birnbaum, A. A. Maryott, and P. F. Wacker, J. Chem. Phys. **22**, 1782 (1954).
[77] I. R. Dagg, in *Phenomena Induced by Intermolecular Interactions*, edited by G. Birnbaum (Plenum, New York, 1985), p. 95.
[78] G. Birnbaum, 1985, cited by K. L. C. Hunt, in *Phenomena Induced by Intermolecular Interactions*, edited by G. Birnbaum (Plenum, New York, 1985), p. 1.
[79] E. B. Wilson, J. C. Decius, and P. C. Cross, *Molecular Vibrations* (McGraw-Hill, New York, 1955).
[80] F. R. W. McCourt and W.-K. Liu, Faraday Disc. Chem. Soc. **73**, 241 (1982).
[81] F. R. W. McCourt and W.-K. Liu, J. Chem. Soc. Faraday Trans. 2 **83**, 387 (1987).
[82] C. J. Jameson, Chem. Rev. **91**, 1375 (1991).
[83] R. D. Amos and M. B. Battaglia, Mol. Phys. **36**, 1517 (1978).
[84] C. J. Jameson, A. K. Jameson, N. C. Smith, and K. Jackowski, J. Chem. Phys. **86**, 2717 (1987).
[85] P. Etesse, J. A. Zega, and R. Kobayashi, J. Chem. Phys. **97**, 2022 (1992).
[86] C. J. Jameson, A. K. Jameson, and M. A. ter Horst, J. Chem. Phys. **95**, 5799 (1991).
[87] C. J. Jameson and A. K. Jameson, J. Chem. Phys. **93**, 3237 (1990).
[88] C. F. Roche, A. Ernesti, J. M. Hutson, and A. S. Dickinson, J. Chem. Phys. **104**, 2156 (1996).